eprints@whiterose.ac.uk
https://eprints.whiterose.ac.uk/

Particle acceleration and non-thermal emission in colliding-wind binary systems

J. M. Pittard[1]⋆, G. E. Romero[2] and G. S. Vila[2]†
[1]*School of Physics and Astronomy, University of Leeds, Woodhouse Lane, Leeds LS2 9JT, UK*
[2]*Instituto Argentino de Radioastronomía, CCT-La Plata, CONICET, 1900FWA, La Plata, Argentina*

ABSTRACT

We present a model for the creation of non-thermal particles via diffusive shock acceleration in a colliding-wind binary. Our model accounts for the oblique nature of the global shocks bounding the wind-wind collision region and the finite velocity of the scattering centres to the gas. It also includes magnetic field amplification by the cosmic ray induced streaming instability and the dynamical back reaction of the amplified field. We assume that the injection of the ions and electrons is independent of the shock obliquity and that the scattering centres move relative to the fluid at the Alfvén velocity (resulting in steeper non-thermal particle distributions). We find that the Mach number, Alfvénic Mach number, and transverse field strength vary strongly along and between the shocks, resulting in significant and non-linear variations in the particle acceleration efficiency and shock nature (turbulent vs. non-turbulent). We find much reduced compression ratios at the oblique shocks in most of our models compared to our earlier work, though total gas compression ratios that exceed 20 can still be obtained in certain situations. We also investigate the dependence of the non-thermal emission on the stellar separation and determine when emission from secondary electrons becomes important. We finish by applying our model to WR 146, one of the brightest colliding wind binaries in the radio band. We are able to match the observed radio emission and find that roughly 30 per cent of the wind power at the shocks is channelled into non-thermal particles.

Key words: binaries: general – gamma-rays: stars – radiation mechanisms: non-thermal – stars: early-type – stars: winds, outflows – stars: Wolf-Rayet

1 INTRODUCTION

Colliding-wind binary (CWB) systems typically consist of two early-type stars whose individual winds collide at supersonic speeds (e.g., Stevens, Blondin & Pollock 1992; Pittard 2009). This interaction produces a wind-wind collision region (WCR) where strong global shocks slow the winds and heat the plasma up to temperatures of 10^7 K or more. The WCR may radiate strongly at X-ray energies, the most famous examples perhaps being WR 140 (e.g., Pollock et al. 2005; Sugawara et al. 2015) and η Carinae (e.g., Hamaguchi et al. 2007; Henley et al. 2008; Corcoran et al. 2010; Hamaguchi et al. 2014a,b, 2016, 2018). Numerical simulations of the X-ray emission from the WCR have become increasingly sophisticated in recent years (e.g., Pittard & Parkin 2010; Parkin & Gosset 2011; Parkin et al. 2011, 2014).

Particles may also be accelerated to high energies at the global shocks bounding the WCR through diffusive shock acceleration (DSA). The presence of such non-thermal particles is revealed by synchrotron emission, which is sometimes spatially resolved (e.g., Williams et al. 1997; Dougherty, Williams & Pollacco 2000; Dougherty et al. 2005; O'Connor et al. 2005; Dougherty & Pittard

2006; Ortiz-León et al. 2011; Benaglia et al. 2015; Brookes 2016) or shows orbital variability (e.g., Blomme et al. 2013, 2017). Catalogues of particle-accelerating CWB systems have been assembled by De Becker & Raucq (2013) and De Becker et al. (2017).

The convincing detection of non-thermal emission at X-ray and γ-ray energies has proved far more difficult, but at last this appears to be changing. In 2018, non-thermal X-ray emission was reported from η Carinae (Hamaguchi et al. 2018). Crucially, the detection was made using NuSTAR, a focusing telescope, which localised the emission to within a few arc-seconds of the binary and revealed that the emission varied with the orbital phase. This work provided much needed confirmation of previous GeV detections (e.g., Reitberger et al. 2015) which suffered from poor localisation. Most recently, η Carinae has been detected at energies of 100's GeV by the HESS telescope (H.E.S.S. collaboration 2020).

Driven by these observations we are developing a numerical model for simulating the non-thermal emission from CWBs. In this paper we take the model presented in Pittard, Vila & Romero (2020) and improve it in several ways. Firstly, the particle acceleration scheme is updated to that in Grimaldo et al. (2019), which generalizes Caprioli et al. (2009)'s model for the case of oblique shocks where the background magnetic field has also a transverse component. This scheme self-consistently includes magnetic field amplification due to the cosmic ray induced streaming instability, and the dynamical back

⋆ E-mail: j.m.pittard@leeds.ac.uk
† Currently at CONICET in YPF Tecnología S.A.

Table 1. The stellar parameters used in our standard model. Both stars are assumed to have an effective temperature $T = 40,000$ K, a surface magnetic field flux density $B_* = 100$ G, and an equatorial rotational speed of 200 km s^{-1}. Both winds are assumed to be clumpy with a volume filling factor $f = 0.1$. The stellar separation, $D = 2 \times 10^{15}$ cm.

Parameter	WR-star	O-star
$\dot{M}$ (M$_\odot$ yr^{-1})	2×10^{-5}	2×10^{-6}
v_∞ (km s^{-1})	2000	2000
L (L$_\odot$)	2×10^5	5×10^5

reaction of the amplified magnetic field. The back reaction reduces the modification of the shock precursor and the total compression ratio of the shock, compared to standard non-linear DSA. However, we improve Grimaldo et al. (2019)'s model by also considering the finite velocity of the scattering centres relative to the fluid. This can have a big effect on the steepness of the non-thermal particle distributions.

Secondly, we include a model for the magnetic field in the stellar winds. Two possible configurations are considered: radial (applicable for non-rotating stars) or toriodal (applicable for rotating stars). Thirdly, the creation of secondary particles from proton-proton interactions is also taken into account. Finally, additional emission and absorption processes are modelled: synchrotron emission, two-photon absorption from the creation of electron-positron pairs, and free-free absorption from the clumpy winds. In Sec. 2 we describe our new model and in Sec. 3 we present the results. We apply our model to the radio bright CWB WR 146 in Sec. 4 and we summarize and conclude in Sec. 5. Further details of some of the improvements to the model are described in a set of Appendices.

2 THE MODEL

2.1 Global structure and upstream quantities

Our model is based on the one presented in Pittard et al. (2020). The reader is referred to this paper for full details, but in brief it is assumed that the stellar winds collide at fixed speeds to create an axisymmetric WCR. Orbital effects and the acceleration/deceleration of the winds are ignored, so our models are currently most appropriate for wide binaries with long orbital periods where these neglected effects are minimised. We also assume that the global shocks are coincident with the contact discontinuity (CD) between the winds, which is a suitable first-order approximation[1]. The position of the CD is computed using the equations in Cantó, Raga & Wilkin (1996), which gives an accurate determination of the half-opening angle for wind momentum ratios > 0.01 (Pittard & Dawson 2018).

Particle acceleration at the shock depends strongly on the assumed pre-shock magnetic field. Close to each star the magnetic field is a dipole; it changes to a radial configuration at distances beyond the Alfvén radius, r_A, and, if the star is rotating, the field lines wrap up and the field becomes toroidal at distances $r > R_* v_\infty / v_{rot}$, where v_{rot} is the equatorial rotation speed of the star, v_∞ is the wind speed and R_* is the stellar radius (Eichler & Usov 1993). The radial field is

$$B(r) = B_* \left(\frac{R_*}{r} \right)^2, \tag{1}$$

---

[1] Pittard & Dawson (2018) determined that the shocks flare away from the CD at angles of $\approx 20°$ when the WCR is largely adiabatic.

where B_* is the magnetic flux density at the stellar surface. For the toroidal field we adopt

$$B_\phi(r, \theta) = B_* \frac{v_{rot}}{v_\infty} \left(\frac{R_*}{r} \right)^2 \left(\frac{r}{R_*} - 1 \right) \sin \theta, \tag{2}$$

where θ is the polar angle, and $B_r = B_\theta = 0$ (see, e.g., García-Segura 1997). We adopt $B_* = 100$ G and $v_{rot}/v_\infty = 0.1$ as reasonable values (see, e.g., Eichler & Usov 1993).

Starting at the apex of the WCR the CD is divided into a sequence of annuli of 1 degree interval in the angle θ measured from the secondary star (hereafter assumed to be the star with the less powerful wind - see, e.g., Fig. 1 in Pittard et al. 2020). Each annulus is then subdivided into 8 segments equally spaced in azimuthal angle Φ, which measures the position on the WCR relative to the rotation axis of each star (the latter are assumed to be aligned with the orbital axis). $\Phi = 0$ points upwards, while $\Phi = \pi/2$ lies in the orbital plane. Φ increases in a clockwise direction for each star. Therefore, particular values for θ and Φ correspond to a particular position on the WCR for each star (although given the definition of Φ the points on each shock will be in opposite halves of the model). The centre of each segment has $\Phi = (2n - 1)\pi/8$ where $n = 1...8$[2].

At the centre point of each segment the pre-shock wind properties are calculated: the density, ρ_0, the velocity parallel ($u_{0\parallel}$) and perpendicular ($u_{0\perp}$) to the CD, and the magnetic field flux density B_0 and angle to the shock normal θ_{B0}. We set the pre-shock gas temperature to $T_0 = 10^4$ K, as appropriate for photoionized stellar winds.

2.2 The shock solution

The non-thermal particle spectrum at the shock is calculated by solving the diffusion-advection equation, as detailed in Appendix A, which provides all quantities of interest. The shock has a precursor and a subshock. All of the far upstream quantities have a subscript "0". Those immediately upstream of the subshock have a subscript "1", while the postshock quantites have a subscript "2". In solving the diffusion-advection equation we assume that all quantities change locally only in the x-direction which is perpendicular to the shock and that the magnetic field lies in the x-z plane.

Four compression factors are of interest. The first two relate to the gas and are $R_{tot} = u_{0x}/u_{2x}$ and $R_{sub} = u_{1x}/u_{2x}$. The second two relate to the scattering centres and are S_{sub} and S_{tot}. The non-thermal particles produce turbulence created by resonant and non-resonant instabilities. If the turbulence is assumed to be Alfvén waves (produced by resonant instabilities) the scattering center speed is the Alfvén speed. However, the nature of the turbulence created by non-resonant cosmic ray current-driven instabilites is significantly different to Alfvén waves, and is not necessarily well described in such terms. Using a Monte Carlo simulation of DSA, Bykov et al. (2014) found that the velocity of the scattering centres relative to the fluid was significantly below the Alfvén speed. However, this is a complicated issue, that might well depend on the level of turbulence upstream, something that is expected to be high in line-driven stellar winds. Therefore, for the time being, we continue to make the standard assumption that the scattering centres move relative to the fluid at the Alfvén velocity, v_A. The compression ratios experienced by the scattering centres are then

$$S_{sub} = \frac{u_{1x} - v_{A1}}{u_{2x} + v_{A2}} \quad \text{and} \quad S_{tot} = \frac{u_{0x} - v_{A0}}{u_{2x} + v_{A2}}. \tag{3}$$

---

[2] In some of the following figures the shock properties and particle distributions are given at other specific values of Φ.

The non-thermal proton distribution function, $f_p(p) = f_1(p) = f_2(p)$, at each position on the shocks is obtained (see Eq. A7). Various pressures are also obtained: the gas thermal pressure, the gas ram pressure, the cosmic-ray pressure, the pressure of the uniform magnetic field, and the pressure of the magnetic waves. The solution also reveals the fraction of the input energy flux that goes into cosmic rays that are either advected downstream or escape upstream (see Eq. A17). The sum of these fractions gives the total fraction going into cosmic rays.

2.2.1 Shock obliquity and particle injection

The 1D kinetic treatment developed by Blasi and collaborators (Blasi 2002; Amato & Blasi 2005, 2006; Caprioli et al. 2009) assumes that the shock is parallel, with the upstream magnetic field aligned with the shock normal. Grimaldo et al. (2019) modified their solution to include a pressure term for the uniform background field, but did not consider how the DSA efficiency changes with the obliquity of the shock. This is a fundamental issue that unfortunately is not yet fully resolved. On the one hand, simulations by Caprioli & Spitovsky (2014) using a hybrid particle-in-cell code show that ion acceleration becomes very inefficient for shock obliquities $\theta_{B0} \gtrsim 45°$, as very few of the reflected ions are able to move further upstream to be injected into the DSA process (Caprioli, Pop & Spitovsky 2015). On the other hand, Reville & Bell (2013) suggested that there exists a quasi-universal shock behaviour, whatever the orientation of the far upstream field, because the field in the immediate upstream region becomes completely disordered. In addition, van Marle, Casse & Marcowith (2018) find efficient DSA for large shock obliquities because the shock becomes corrugated (though Haggerty & Caprioli (2019) disagree with these findings). Furthermore, large $(\delta B/B_0)$ Alfvénic turbulence upstream may allow injection of ions at shocks that are perpendicular on average (Giacalone 2005), although for this process to be efficient the fluctuations must be strong on length-scales comparable to the gyroradius of suprathermal particles (see the discussion in Caprioli, Zhang & Spitovsky 2018).

The injection of electrons into the DSA process has long been an outstanding problem but this is beginning to be tackled through simulations that now show the simultaneous acceleration of both electrons and ions (Park, Caprioli & Spitkovsky 2015; Kato 2015). In quasi-parallel shocks, electrons are not efficiently accelerated and the fraction of the shock energy that goes into them, $\zeta_e \lesssim 10^{-3}$. On the other hand, Xu, Spitkovsky & Caprioli (2020) find that electrons are efficiently injected and accelerated via shock-drift acceleration and then DSA in quasi-perpendicular shocks ($\theta_{B0} = 63°$) if M and (particularly) M_A are high enough. In such cases $\zeta_e \sim 0.1$. Thus it might be the case that some shocks preferentially accelerate electrons and not ions.

Faced with this current understanding there are two extreme positions that can be taken with any model:

(i) If the flow at the shock is strongly turbulent on small scales (perhaps because of turbulence far upstream), or if the shock becomes corrugated, then the electron and ion acceleration efficiency may be independent of the shock obliquity, with ions accelerated more efficiently than electrons.

(ii) If not, then quasi-perpendicular shocks may accelerate electrons efficiently but not ions (with no significant shock modification), while quasi-parallel shocks may accelerate ions efficiently (with significant shock modification) but not electrons.

In the current work we adopt the former scenario in which the ion acceleration efficiency is dependent on M, M_A and the maximum

momentum of the non-thermal protons, p_{max}, but not on θ_{B0} (in particular, the value of χ in Eq. A5 is kept fixed and independent of θ_{B0}). This might be consistent with the known clumpy nature of line-driven stellar winds. In future work we will explore the second possibility.

2.2.2 Maximum proton momentum

The solution to the diffusion-advection equation depends on p_{max}, which generally depends on geometrical (Hillas 1984) or temporal (Lagage & Cesarsky 1983) conditions[3]. In exceptional circumstances p_{max} can be set by proton-proton losses (as occurs in η Carinae; White et al. 2020), but this is not important in the models in the current work where we find the geometrical condition dominates. p_{max} is thus set by the diffusion (escape) of particles from the shock, where the diffusion length $l_{diff} = r_{shk}/4$, and where r_{shk} is the distance of the shock from the star. This gives a maximum proton energy $E_{max} = l_{diff} e B_0 u_{0\perp}/c$, where e is the proton/electron charge. As in Ellison, Decourchelle & Ballet (2004), a turnover is applied to the distribution at the highest energies, according to

$$\exp\left[-\frac{1}{\alpha}\left(\frac{p}{p_{max}}\right)^{\alpha}\right], \tag{4}$$

where α is a constant. Steeper turndowns are achieved with higher values of α, and in this work we adopt $\alpha = 4$ ($\alpha = 1$ was used in Pittard et al. 2020). This change was necessary in order for the synchrotron emission to fall below the thermal X-ray flux in our model of WR 146 (see Sec. 4). Values of α as high as 4 have been previously used in the literature (see Ellison et al. 2004).

2.2.3 Maximum electron momentum

The non-thermal electron distribution function, $f_e(p)$, is not an output from the solution to the diffusion-advection equation. In keeping with usual practice we set $f_e(p) = K_{ep} f_p(p)$, with an exponential cut-off at $p_{max,e}$ that is set by radiative losses. We assume that $K_{ep} = 0.01$ (as in Pittard & Dougherty 2006; Pittard et al. 2020). Though the value of K_{ep} is not yet well measured or constrained in CWBs, the value we use is consistent with the well-established ratio of proton to electron energy densities for Galactic cosmic rays of ~ 100 (Longair 1994), and is in rough agreement with observations of young Galactic SNRs (e.g., Morlino & Caprioli 2012) and simulations (e.g., Park et al. 2015) that find $K_{ep} \approx 10^{-3} - 10^{-2}$.

The non-thermal electron distribution is also prevented from exceeding the Maxwell-Boltzmann thermal distribution, which can occur when the former has a very steep slope. In such cases we locally reduce the value of K_{ep} and the normalization of $f_e(p)$ so that it matches and smoothly connects to the peak of the Maxwell-Boltzmann thermal distribution (cf. Fig. 1 in Caprioli et al. 2010).

The value of $p_{max,e}$ is calculated by balancing the local acceleration and loss rates. For $\gamma \gg 1$, the electron acceleration rate is given by (see Eq. 6 in Pittard et al. 2006)

$$\frac{d\gamma_e}{dt} = \frac{8}{9}\frac{R_{sub} - 1}{R_{sub}}\frac{u^2}{c^2}\frac{eB}{m_e c}, \tag{5}$$

---

[3] If the escaping cosmic rays are able to self-confine by creating upstream magnetic turbulence, the maximum cosmic ray energy may become independent of the strength of the ambient magnetic field, and instead depend on the time taken for the magnetic field to be amplified (Bell et al. 2013). This possibility is not considered in our model.

where u is the shock velocity ($u = u_{0\perp}$), and we have assumed that the non-thermal electrons feel a compression factor R_{sub}[4]. We further assume that u and B take their *pre-subshock* values ($u = u_1$ and $B = B_1$). The loss rates are given in Appendix A of Pittard et al. (2020). For the synchrotron loss rate we use the *total* (normal plus turbulent) *post-shock* magnetic field i.e. $B = B_{2,tot} = \sqrt{B_2^2 + (\delta B_2)^2}$, where B_2 and δB_2 are the magnetic flux densities of the postshock uniform and turbulent fields, respectively. This yields a slightly lower maximum energy for the primary non-thermal electrons and their emission, compared to using only the non-turbulent component of the magnetic flux density. The total magnetic flux density is also used for the downstream synchrotron cooling and emission.

At relatively close stellar separations (e.g., $D_{sep} \lesssim 10^{14}$ cm), $p_{max,e}$ will typically be set by inverse Compton losses which will occur in the Thomson limit. However, in wider systems the inverse Compton losses will be reduced by the Klein-Nishina effect so that synchrotron cooling may become the dominant energy loss mechanism. The cooling time as a function of electron energy for various processes is shown in Fig. 6 of Pittard et al. (2020).

2.3 The downstream solution

The non-thermal particle spectrum downstream of the shock is calculated by solving the kinetic equation. For a volume co-moving with the underlying thermal gas, and ignoring diffusion and particle escape, the energy distribution $n \equiv dN/dE$ as a function of time t and energy E is given by the continuity equation (Ginzburg & Syrovatskii 1964; Blumenthal & Gould 1970):

$$\frac{\partial n(E,t)}{\partial t} + \frac{\partial(\dot{E}n(E,t))}{\partial E} = Q(E,t). \tag{6}$$

The second term is an advection term in energy space due to cooling processes and this equation is valid when the energy losses can be treated as continuous (for further details see Appendix A in Pittard et al. 2020). $Q(E,t)$ is the number of particles per unit volume injected in a time dt in the energy range ($E, E + dE$); the addition of this term marks an important difference from our previous work (cf. Pittard et al. 2020), where we did not include it. Our calculation of the injection function for secondary electrons (actually electron-positron pairs), $Q_{e\pm}$, is detailed in Appendix B. The secondary electrons are produced via the decay of charged pions, which are created in collisions between thermal and non-thermal protons. The creation of secondary electrons by interactions between photons and non-thermal protons is detailed in Appendix C. We show in Appendix D that proton-proton interactions dominate the emissivity in our standard CWB model, justifying our omission of interactions between non-thermal protons and stellar photons.

The fluid properties are assumed to be constant within each segment on the WCR. When the co-moving volume containing the thermal and non-thermal particles moves along the CD and into the next segment the fluid properties are set to those of the new segment. This leads to a steady decrease in the gas density and temperature and the magnetic flux density and a steady increase in the velocity. The photon energy density from the stars also drops. The number density of the non-thermal particles is also reduced through the relative

adiabatic expansion between the two segments (cf. Appendix A in Pittard et al. 2020).

2.4 Further details

Our new model also includes synchrotron emission, and photon-photon and free-free absorption. Details of the calculation of the synchrotron emission are provided in Appendix E. The absorption of high energy photons by collisions with stellar photons to create electron-positron pairs is detailed in Appendix F[5]. The free-free absorption of low energy photons is detailed in Appendix G. A final change to our previous model is the use of the Khangulyan, Aharonian & Kelner (2014) approximation for the inverse Compton emissivity when the target photons have a black-body distribution (see also del Palacio et al. 2020). This removes one loop from the calculations and leads to a significant speed-up with no loss of accuracy.

3 RESULTS

Unless otherwise noted we adopt a set of "standard" parameters for our model, in which the stellar separation is $D = 2 \times 10^{15}$ cm and the viewing angle $\phi = 90°$ (i.e. the line-of-sight is perpendicular to the line-of-centres between the stars - see also Fig. 1 in Pittard et al. 2020). Other parameters of our model are noted in Table 1. The model is not of any particular system, but its parameter values are chosen to be representative of a WR+O system with a reasonably wide stellar separation. For simplicity the DSA model assumes that the winds are pure hydrogen, but all other parts of the code use WC mass fractions ($X = 0.0, Y = 0.5, Z = 0.5$) for the WR-star and solar mass fractions ($X = 0.7381, Y = 0.2485, Z = 0.0134$; Grevesse et al. 2010) for the O-star. The wind momentum ratio is 0.1 and the stagnation point is at a distance of 0.26 D from the O-star, where D is the stellar separation. The WCR is largely adiabatic. Numerical values of some pre-shock quantities are given in Sec. 2.7 of Pittard et al. (2020). With a toriodal magnetic field in the wind of each star, the pre-shock magnetic flux density on the line of centres is 4 mG for the WR-shock and 20 mG for the O-shock. The shocks are almost perpendicular at this location.

3.1 The standard model

3.1.1 Quantities along each shock

Fig. 1 shows various quantites from our standard model as a function of angle, θ, along the CD as measured from the secondary star ($\theta = 0°$ corresponds to the stagnation point of the WCR on the line-of-centres between the stars, while $\theta = 90°$ indicates a point on the CD where

---

[4] Electrons confined to the sub-shock will feel a compression ratio given by S_{sub}, but those with higher energy will stream further upstream and downstream and will feel slightly greater compression. Our choice of R_{sub} is supposed to mimic this as often R_{sub} is slightly greater than S_{sub}.

[5] The emission from such pairs is currently not calculated. Nor do we consider the possibility of an inverse Compton pair cascade (e.g., Bednarek 2005; Khangulyan, Aharonian & Bosch-Ramon 2008). For an inverse Compton cascade to develop, inverse Compton energy losses must dominate over synchrotron energy losses (as seen in Fig. 6 of Pittard et al. 2020). Assuming a toroidal magnetic field in the stellar winds, the spectrum up to TeV energies will be affected if the surface magnetic field, $B_* \lesssim 5 \frac{L_5^{0.5}}{R_{10}} \frac{v_\infty}{v_{rot}}$, where L_5 is the stellar luminosity in units of 10^5 $L_\odot$ and R_{10} is the stellar radius in units of 10 $R_\odot$. Note that there is no dependence on the distance to the star(s). With our standard model parameters we obtain $B_* \lesssim 150$ G. Thus pair cascades can be expected to develop in CWB systems when the optical depth for γ-γ absorption becomes significant (which requires $D \lesssim 10^{13}$ cm for our standard model parameters - see Fig. 10).
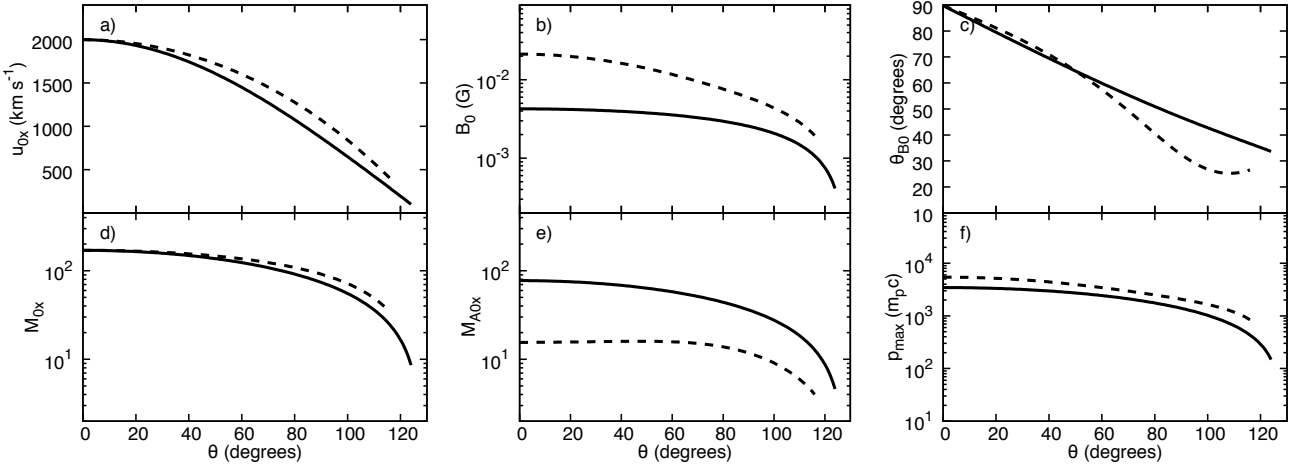
Figure 1. Selected quantities along the CD as a function of the angle θ from the secondary star (see Fig. 1 in Pittard et al. (2020) for the definition of θ). Panels a-f) show the upstream perpendicular wind velocity (u_{0x}), magnetic flux density (B_0), angle of the magnetic field to the shock normal (θ_{B0}), perpendicular Mach number (M_{0x}), perpendicular Alfvénic Mach number (M_{A0x}), and the maximum non-thermal proton momentum (p_{max}). In all panels the solid line indicates the properties for the WR-shock, while the dashed line indicates the properties for the O-shock. B_0, θ_{B0}, M_{A0x} and p_{max} are all dependent on the azimuthal angle of the position on the WCR. The values in this figure are for $\Phi = \pi/4$.
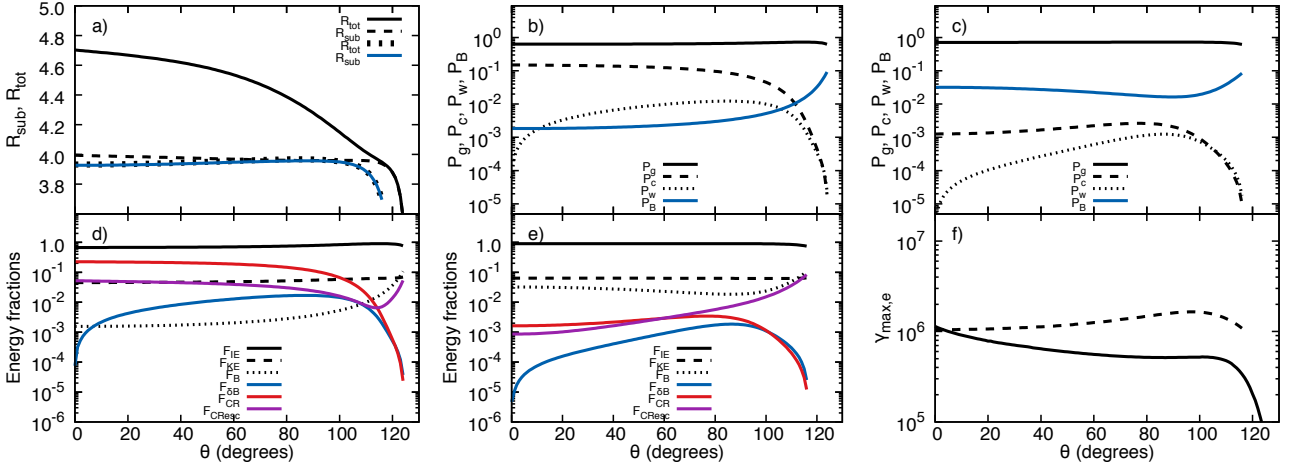

Figure 2. Selected quantities along the CD as a function of the angle θ from the secondary star. Panel a) shows the gas compression ratio across the subshock (R_{sub}) and the entire shock (R_{tot}). The properties for the WR-shock are shown by the black solid and dashed lines. The properties for the O-shock are shown by the black dotted and blue solid lines. Panels b) and c) show the postshock pressure (normalized to $\rho_0 u_{0x}^2$) for the gas (P_g), cosmic rays (P_c), magnetic turbulence (P_w) and uniform magnetic field (P_B). Panel b) shows the properties for the WR-shock while panel c) shows the properties for the O-shock. Panels d) and e) show the downstream thermal (F_{IE}), kinetic (F_{KE}), magnetic (F_B), magnetic turbulence ($F_{\delta B}$) and cosmic ray (F_{CR}) energy fractions. F_{CResc} is the fraction of energy in the cosmic rays that escape upstream of the shock. The total energy fraction of the cosmic rays is $F_{CR} + F_{CResc}$. Panel d) shows the properties for the WR-shock while panel e) shows the properties for the O-shock. Panel f) shows the maximum Lorentz factor of the non-thermal electrons from the WR-shock (solid) and the O-shock (dashed) (the maximum proton momentum is shown in Fig.1). The values in this figure are for $\Phi = \pi/4$.

$z = D$ - see Fig. 1 in Pittard et al. (2020)). The maximum value of θ is 180° minus the half-opening angle of the WCR. For our standard parameters, the half-opening angle is $\approx 50°$, so $\theta_{max} \approx 130°$.

Fig. 1a) shows that the perpendicular pre-shock velocity is equal to 2000 km s^{-1} on the axis of symmetry of the WCR (i.e. at the stagnation point between the winds), but steadily declines as one moves off-axis. The WR-shock becomes more oblique more rapidly than the O-shock. $u_{0x} = u_{0\perp} \to 0$ as $\theta \to \theta_{max}$.

Fig. 1b) shows that the pre-shock magnetic flux density is significantly higher for the O-shock than for the WR-shock. This mainly reflects the fact that the WCR is much closer to the O-star, though there is also some enhancement due to the larger radius of the O-star. This is a key difference to our previous work (Dougherty et al. 2003;

Pittard et al. 2006; Pittard & Dougherty 2006; Pittard et al. 2020) where the on-axis pre-shock magnetic flux density was assumed to be identical for both winds.

The angle that the pre-shock magnetic field makes to the shock normal, θ_{B0}, is nearly 90° near the stagnation point (i.e. the shock is very nearly perpendicular - see Fig. 1c). As one moves off-axis the field becomes more oblique. Note that the value of θ_{B0} is a function of both θ and Φ. Thus the particle acceleration is no longer azimuthally symmetric if the stars are rotating and the pre-shock magnetic field is toriodal. In such a case the shock is always perpendicular when $\Phi = 0$ or π (for all values of θ). However, while it starts off perpendicular when $\Phi = \pi/2$ (when $\theta = 0°$), it becomes more and more oblique as θ increases.
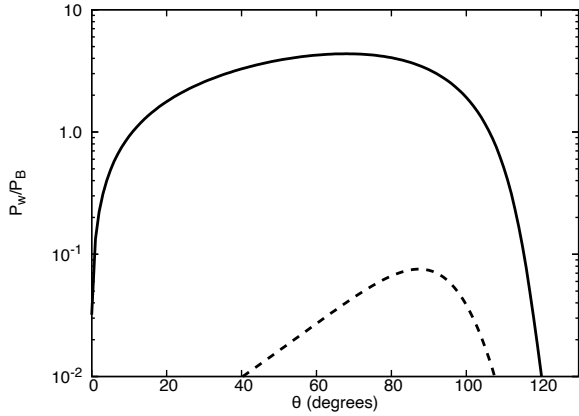
Figure 3. Ratio of the turbulent to non-turbulent magnetic field as a function of angle (position) along the contact discontinuity. The properties of the WR-shock are shown by the solid line while the dotted line shows the properties of the O-shock. The post-shock magnetic field is turbulent for most of the WR-side of the CD, but is more ordered on the O-side.

Fig. 1d) shows that the pre-shock perpendicular Mach number is above 100 for both shocks up to $\theta \approx 90°$. The pre-shock perpendicular Alfvénic Mach number is a factor of two lower than M_{0x} for the WR-shock, but for the O-shock $M_{A0x} \sim 0.1 M_{0x}$, so that $M_{A0x} \lesssim 15$ (Fig. 1e). As we will see, this drastically affects the particle acceleration efficiency of the O-shock in the standard model.

Fig. 1f) shows that the maximum non-thermal proton momentum is nearly twice as high for the O-shock. This is because the stronger magnetic field more than compensates for the reduced radius of the shock.

While the focus of Fig. 1 is mostly on pre-shock quantities along each shock, the focus of Fig. 2 is mostly on the post-shock quantities. It is immediately clear from the values of $R_{tot} > 4$ that the WR-shock is an efficient accelerator of non-thermal particles (until $\theta \gtrsim 110°$), while the O-shock is not (see Fig. 2a). The reason for this is due to the different values of M_{A0x} for the two shocks. When M_{A0x} is small enough, the compression ratios felt by the non-thermal particles (S_{sub} and S_{tot}; see Eq. 3) can become significantly lower than that felt by the fluid (R_{sub} and R_{tot}). This leads to a steeper spectral slope for the non-thermal particles, as noted by Bell (1978). This is discussed further in Sec. 3.1.3.

Fig. 2b) shows the various post-shock pressures, normalized to the pre-shock ram pressure, for the WR-shock. The thermal gas pressure still dominates but the cosmic ray pressure remains above 10% until $\theta > 80°$. The accelerated particles are also able to generate significant magnetic turbulence. Along a significant part of the WR-shock the turbulent field exceeds the uniform field, by up to a factor of 2. In contrast, the post-shock pressure from the non-turbulent magnetic field is the second most important pressure behind the O-shock (Fig. 2c), and the pressure from the turbulent field is lower. This means that the post-shock magnetic field is turbulent for most of the WR-side of the CD, but is more ordered on the O-side (see Fig. 3).

The WR-shock manages to convert 20% of the input energy flux into cosmic rays that are advected downstream (Fig. 2d). A further 5% goes into cosmic rays that escape upstream. In contrast, the O-shock puts < 1% of the incoming energy flux into downstream cosmic rays (nearly 10% goes into cosmic rays that escape upstream as $\theta \rightarrow \theta_{max}$, but there is very little energy going into the shock at this stage). Thus the non-thermal particles accelerated at the WR-shock will dominate the non-thermal emission, as we show in Sec. 3.1.4.

Table 2. The value of x_* in our standard model, as a function of θ and Φ. The stellar separation, $D = 2 \times 10^{15}$ cm.

θ (°)	Φ (°)	x_* (cm)	
		WR-shock	O-shock
0.5	$\pi/4$	2.7×10^{13}	1.0×10^{13}
0.5	$\pi/2$	2.7×10^{13}	1.0×10^{13}
90.5	$\pi/4$	1.1×10^{14}	8.0×10^{13}
90.5	$\pi/2$	1.6×10^{14}	8.0×10^{13}
110.5	$\pi/4$	2.2×10^{14}	1.9×10^{14}
110.5	$\pi/2$	3.1×10^{14}	2.1×10^{14}

Fig. 2f) shows that radiative losses limit the maximum Lorentz factor of the non-thermal electrons to $\gamma_{max,e} \sim 10^6$ (for the protons $\gamma_{max} \gtrsim 10^3$). This is slightly lower than in Pittard et al. (2020). Part of it is due to the stronger synchrotron losses that are now assumed (i.e. the use of $B_{2,tot}$ rather than B_0). The change in $\gamma_{max,e}$ with θ reflects the changing pre-shock magnetic field, compression, and generation of the turbulent magnetic field.

3.1.2 The shock precursor

Fig. 4 shows pressure profiles in the WR-shock precursor as a function of position on the WCR. Panels a)-c) are for $\Phi = \pi/4$ while panels d)-f) are for $\Phi = \pi/2$ (i.e. positions on the WCR that lie in the orbital plane). Panels a)-c) show that the normalized cosmic ray pressure drops as θ increases, reflecting the drop in the acceleration efficiency. Note that there is practically no difference between panels a) and d), as the pre-shock magnetic flux density and angle to the shock normal is almost identical. However, there are significant differences between panels c) and f) since there are now much larger differences in B_0 and θ_{B0} at these positions on the WR-shock.

U_{0x} is almost equal to 1.0 for all of the cases in Fig. 4 (the minimum value of $U_{0x} = 0.85$ is obtained for $\theta = 0.5°$). Finally, Fig. 4 shows that while the cosmic ray and turbulent magnetic pressures both increase in the precursor, there is very little increase in the thermal and magnetic pressures (again this is most obvious when $\theta = 0.5°$), indicating that there is little compression and/or heating within the precursor.

Fig. 5 shows the profiles in the precursor of the O-shock. We see again that this shock is far less effective at accelerating particles than the WR-shock, and also that the precursor is less extended. We see that when $\Phi = \pi/4$, the normalized cosmic ray pressure immediately upstream of the subshock, P_{c1}, is roughly constant for $\theta = 0 - 90°$, but drops sharply for $\theta > 90°$ (panels a-c). However, when $\Phi = \pi/2$, P_{c1} drops continuously with θ.

Table 2 notes the values of x_* for each position on the WCR shown in Figs. 4 and 5. Fig. 4 shows that the cosmic rays stream up to distances $\sim 10 x_*$ from the WR-subshock, but are confined to distances $\ll x_*$ from the O-subshock. We see that the cosmic ray precursor is generally much smaller than the local scale of the shock (taken to be $r_{WR}D$ and $r_{OB}D$ for the on-axis ($\theta = 0°$) WR and O-shocks, respectively - for the standard model $r_{WR} = 0.74$ and $r_{OB} = 0.26$ - see also Fig. 1 in Pittard et al. 2020). While the size of the WR-shock precursor relative to the WCR starts to become significant as one moves off-axis, for the most part our use of a 1-dimensional cosmic-ray shock model is valid and appropriate. The far-off-axis region of the WCR adds little to the total cosmic-ray population and emission, in any case.
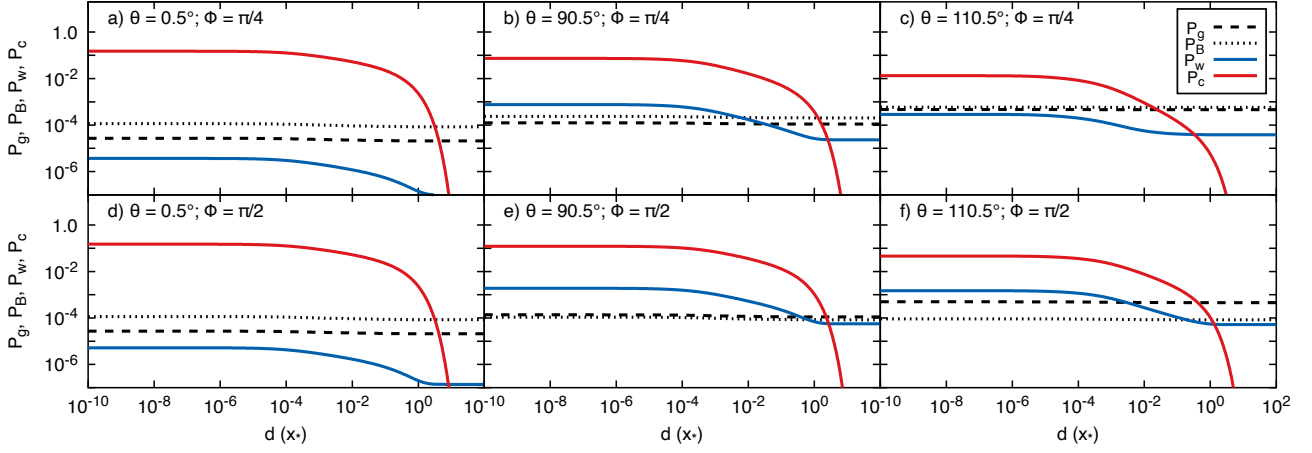
Figure 4. The normalized thermal (P_g), magnetic (P_B), magnetic turbulence (P_w), and cosmic-ray (P_c) pressures in the WR-shock precursor. The subshock is located at the left side of each panel and the upstream flow is incident from the right. The location upstream of the subshock is in units of $x_* = D(p_{max})/u_{0x}$. Each panel shows a different location on the WR-shock front, indicated by the values of θ and Φ. In all cases the normalized perpendicular pre-shock velocity U_x remains close to 1.0 (not shown).
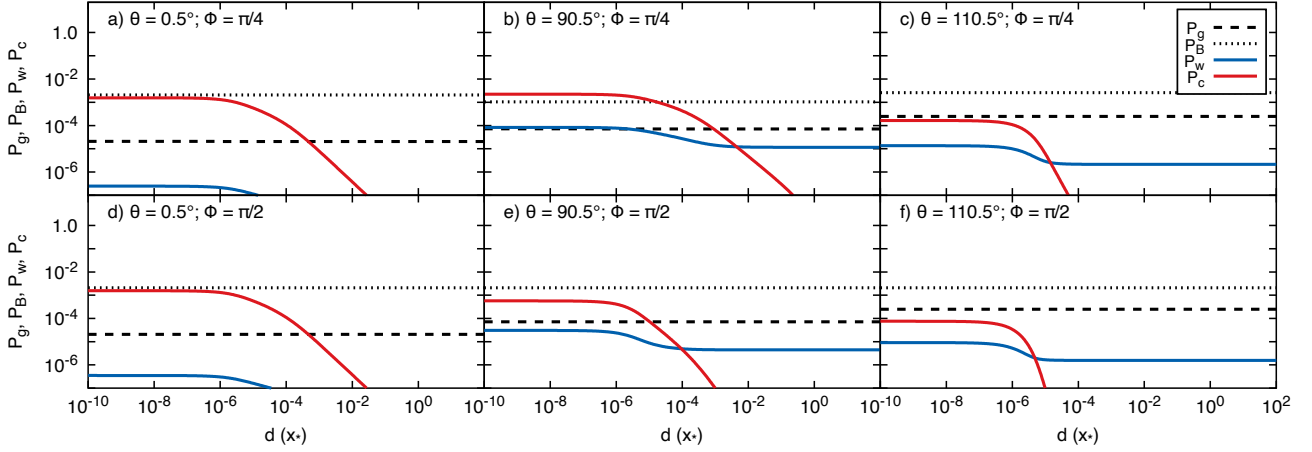

Figure 5. As Fig. 4 but for the O-shock. The precursor is less extended compared to that of the WR-shock (see Fig. 4).

3.1.3 The particle distributions

Figs. 6 and 7 show the distributions of the thermal and non-thermal particles immediately downstream of the subshock. In each figure the proton distributions are indicated by a "p", while the electron distributions are indicated by an "e". The particle distributions are shown for the WR-shock (solid line) and the O-shock (dashed line). Fig. 6 shows the distributions for $\theta = 0°$, while Fig. 7 shows them for $\theta = 110°$. In both cases $\Phi = \pi/4$.

The stand-out feature in both figures is the slope of the non-thermal particle distribution. The spectral index n of the particle distribution ($f(p) \propto p^n$) is given by

$$n = -\frac{3r}{r-1}, \tag{7}$$

where r is the relevant compression ratio. For a strong, non-relativistic shock with polytropic index $\gamma = 5/3$, the density compression ratio is $r = R_{tot} = 4$, which gives $n = -4$ (i.e. a flat distribution in our figures). However, if the scattering centres move relative to the fluid their compression ratio can be reduced, leading to steeper spectra. The on-axis WR-shock has $R_{tot} = 4.7$, $R_{sub} = 3.99$, $S_{tot} = 4.1$ and $S_{sub} = 3.5$. The spectral index of the particle dis-

tribution should therefore vary from $n = -4.2$ at low energies to $n = -3.97$ at high energies, which is indeed consistent with Fig. 6 (the high energy slope is not seen due to the maximum energy cut-off of the particles). For the on-axis O-shock we find $R_{tot} = R_{sub} = 3.93$ but $S_{tot} = S_{sub} = 2.45$. This yields $n = -5.1$ and is again consistent with the displayed distribution.

The stellar parameters of our standard model are not too dissimilar from those used by del Palacio et al. (2016) to model HD 93129A. It is therefore interesting that in order to match the observed synchrotron emission from HD 93129A, del Palacio et al. (2016) adopt an energy index of $p = 3.2$ for the non-thermal particles in their model. This corresponds to $n = -5.2$ for the momentum index of the particles, and is very similar to the index that we find for the particles accelerated at the on-axis O-shock (see Fig. 6). del Palacio et al. (2020) also consider a hardening of the high energy particle distribution to $p = 2$ (equivalent to $n = -4$), which is what we obtain for the WR-shock in our model.

In Fig. 6 the curvature of the non-thermal part of the distributions from the WR-shock reveal some modest shock modification, but it is much reduced compared to the pure hydrodynamic case (cf. Fig. 4
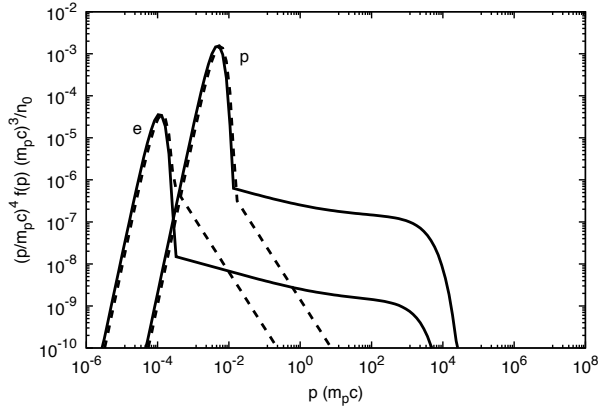
Figure 6. The proton and electron distributions for the WR-shock (solid line) and O-shock (dashed line) for $\theta = 0°$ and $\Phi = \pi/4$. For the WR-shock, $R_{tot} = 4.7$, $R_{sub} = 3.99$, $S_{tot} = 4.1$ and $S_{sub} = 3.5$. For the O-shock, $R_{tot} = R_{sub} = 3.93$ and $S_{tot} = S_{sub} = 2.45$. For both shocks $n_0 = 1.3 \times 10^5$ cm^{-3}. The thermal peaks are visible at low momenta.

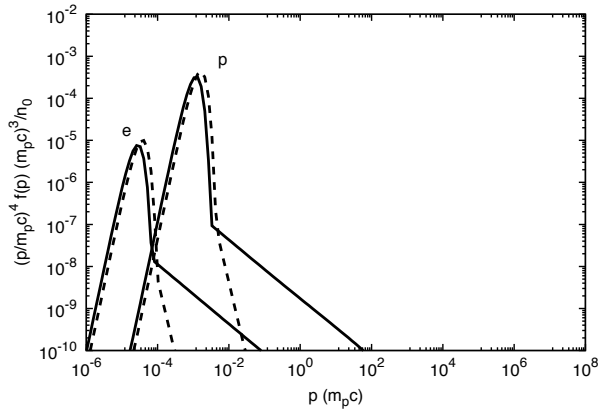**Figure 7.** The proton and electron distributions for the WR-shock (solid line) and O-shock (dashed line) for $\theta = 110°$ and $\Phi = \pi/4$. For the WR-shock, $R_{tot} = 4.02$, $R_{sub} = 3.96$, $S_{tot} = 2.96$ and $S_{sub} = 2.91$. For the O-shock, $R_{tot} = R_{sub} = 3.89$ and $S_{tot} = S_{sub} = 1.99$. For the WR-shock $n_0 = 2.0 \times 10^4$ cm^{-3}, while for the O-shock $n_0 = 4.2 \times 10^3$ cm^{-3}.

in Pittard et al. 2020), and this is also manifest in the shift to higher momenta of the thermal peaks. Fig. 6 again indicates that the particle acceleration at the O-shock is very inefficient. Fig. 7 shows that as θ increases the particle acceleration also becomes inefficient for the WR-shock, with the observed steepening of the particle distribution consistent with $S_{sub} = 2.91$ (giving $n \approx -4.6$). This behaviour again contrasts with Pittard et al. (2020) - see their Fig. 5.

3.1.4 *The non-thermal emission*

The non-thermal emission from our standard model is shown in Fig. 8. The inverse Compton emission dominates at $E \gtrsim 1$ keV while synchrotron emission dominates for $E \lesssim 10$ eV. Free-free absorption by the stellar winds causes the synchrotron emission to turnover at about 2 GHz (which is comparable to the turnover frequency found from the full hydrodynamic models in Pittard et al. 2006). However, the Razin turnover frequency occurs at about 5 GHz and dominates the low frequency turnover in this model. The emission from π^0-decay adds slightly more than 10% to the total emission between
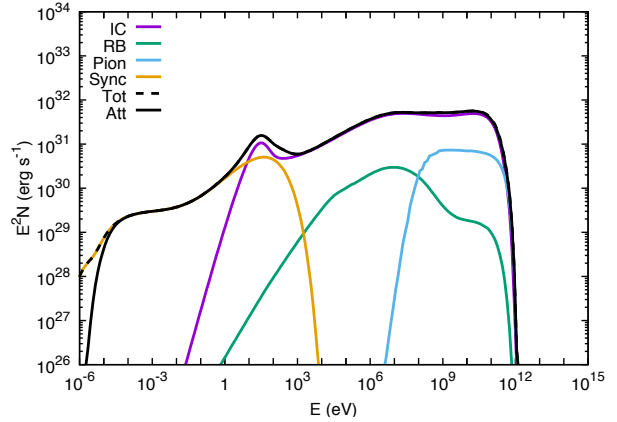

Figure 8. The non-thermal emission from our standard model. The intrinsic emission from the inverse Compton (IC), relativistic bremmstrahlung (RB), π^0-decay (Pion), and the synchrotron (Sync) processes are shown separately, as well as their combined total (Tot) and the total attenuated (Att) emission (which accounts for free-free and photon-photon absorption). The stellar separation $D = 2 \times 10^{15}$ cm and the viewing angle $\phi = 90°$.

0.3 − 100 GeV. The non-thermal emission in Fig. 8 is somewhat softer than that seen in Fig. 10 in Pittard et al. (2020), where a more pronounced upwards curvature in the emission towards higher energies is seen. This is due to the lower compression ratio of the scattering centres which steepens the particle distributions in the current work, and the less strongly modified shocks. The π^0-decay emission is also weaker relative to the inverse Compton emission in the current work, due to the lower total gas compression ratio R_{tot}. γ-γ absorption is negligible.

The spectral shape of the inverse Compton emission around $1 - 10^3$ eV is rather unexpected. Fig. 9 shows that this is due to emission from the particles accelerated at the O-shock, but a "bump" in the emission is also seen from particles accelerated at the WR-shock. Tests show that in both cases this "bump" is produced by electrons with Lorentz factors $\gamma < 2$. It arises due to the cooling experienced by the downstream electrons, which gives rise to a "peaked" particle distribution (see Figs. 6, 7 and 10 in Pittard et al. 2020). Removing the emission from these particles creates a smooth downturn at these energies. Fig. 9 also shows that the total emission is dominated by particles accelerated at the WR-shock, and that the emission from the O-shock is noticeably softer. This is expected given the particle distributions shown in Figs. 6 and 7.

3.2 The effect of varying the stellar separation

Fig. 10 shows how the non-thermal emission changes as the stellar separation is varied. It is clear that the π^0-decay emission increases steadily as D decreases (scaling as D^{-1} - see Pittard et al. 2020). So while the non-thermal spectrum at large D is dominated by synchrotron and inverse Compton emission (at low and high energies, respectively), at closer separations the high energy emission becomes dominated by the γ-rays created by π^0-decay (emission from secondary electrons may also become important - see Sec. 3.4). At $D = 2 \times 10^{17}$ cm the synchrotron emission dominates up to $E = 1$ keV, while at higher energies inverse Compton emission takes over. As D decreases the spectral shape of the synchrotron emission changes quite markedly, due to a softening of the non-thermal electron spectrum. The maximum energy of the inverse Compton emission is $\gtrsim 10^{12}$ eV at $D \gtrsim 10^{15}$ cm, but decreases for closer sep-
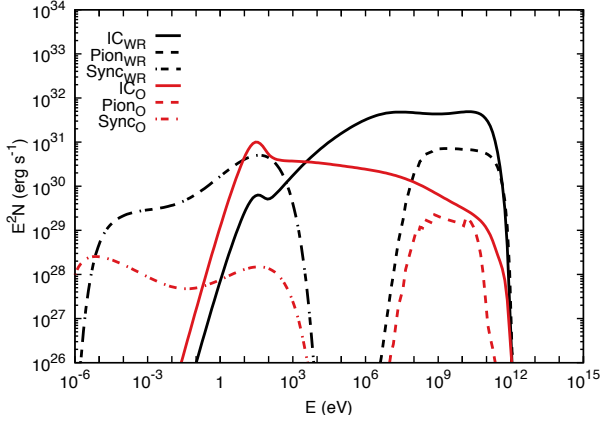
Figure 9. The contribution of each shock to the intrinsic non-thermal emission from our standard model. The emission from particles accelerated by the WR-shock is shown by the black lines, while the emission from the O-shock accelerated particles is shown by the red lines. Except for a narrow range at $\sim 10-100\,\mathrm{eV}$, the WR-shock completely dominates the non-thermal emission.

arations, being $\sim 10^{10}$ eV when $D \sim 10^{13}$ cm. γ-γ absorption only becomes significant at $D \lesssim 10^{14}$ cm.

Pittard et al. (2020) showed that the emission from non-thermal electrons varies in a more complicated way with D. If the cooling length of the non-thermal electrons is greater than or of order the size of the WCR, then they fill the WCR and the emission also varies as D^{-1}. However, if the non-thermal electrons cool more rapidly then the emission will tend towards a constant value (i.e. be independent of D). They also noted that as $p_{\mathrm{max,e}} \propto D^{-1}$ (for an assumed scaling of $B_0 \propto D^{-1}$), this would drive further changes in the emission with D.

Panel f) in Fig. 10 shows the total attenuated non-thermal spectrum at each distance. For $E \gtrsim 10^3$ eV the emission generally increases with decreasing D, though depending upon the energy, the increase is not always steady or even strictly monotonic. As D drops further the emission plateaus, as predicted by Pittard et al. (2020). Free-free absorption by the clumpy stellar winds curtails the low-frequency synchrotron emission as D decreases, with the turnover frequency scaling as $\nu \propto D^{-10/7}$ (Dougherty et al. 2003). The Razin effect produces a characteristic cut-off frequency that is given by $\nu_{\mathrm{R}} = 20 n_{\mathrm{e}}/B$. Since in our standard model $B \propto 1/D$ and $n_{\mathrm{e}} \propto 1/D^2$, the cut-off frequency scales as $\nu_{\mathrm{R}} \propto D^{-1}$. This is responsible for the turndown in the *intrinsic* synchrotron emission seen in Fig. 10.

3.3 The effect of varying the stellar wind magnetic field

The pre-shock magnetic field depends on the strength of the magnetic field at the stellar surfaces, B_*, and the rotation speed of the star, v_{rot}. The latter affects how tightly wound the field-lines are in the equatorial plane of the star. In the extreme case that the stars are not rotating the stellar wind drags the field lines into a radial configuration. In the following we vary both B_* (specifically the surface magnetic field of the O-star, $B_{*\mathrm{O}}$) and v_{rot} to see how each may change the particle acceleration and non-thermal emission.

3.3.1 Changing the surface magnetic field

We first explore changing B_*. Since B_0 is higher for the O-shock than it is for the WR-shock in the standard model (see Fig. 1), we reduce the surface magnetic field strength of the O-star to $B_{*\mathrm{O}} = 10\,\mathrm{G}$ (the

standard model has $B_* = 100\,\mathrm{G}$ for both stars). This results in an on-axis pre-shock magnetic field strength of 2.1 mG and an Alfvénic Mach number of 155 at the O-shock. The result is that the on-axis O-shock becomes much more efficient at accelerating particles than before, with 45% of the incoming kinetic flux now turned into non-thermal particles flowing downstream from the shock. This is a greater efficiency than the on-axis WR-shock (which is at 23%), and is also manifest as a higher compression ratio for the O-shock ($R_{\mathrm{tot}} = 7.2$) in this situation.

We find that the particle acceleration process behaves non-linearly with the magnetic field strength at the shock. As the surface magnetic field of the O-star reduces from 100 G the particle acceleration efficiency at the O-shock first increases and then reduces again. This is because of two competing effects. First, the acceleration efficiency increases as the Alfvénic Mach number of the shock increases. Second, the maximum proton energy decreases ($E_{\mathrm{max}} \propto B_0$ - see Sec. 2.2.2) - this eventually causes the acceleration to become inefficient.

This non-linear behaviour is manifest in the resulting non-thermal emission which is shown in Fig. 11. The dependence of the particle acceleration efficiency on M_{A0x} and p_{max} results in the peak of the synchrotron emission being obtained at an intermediate value of $B_{*\mathrm{O}}$.

Considering the IC emission in Fig. 11b), we see that the IC emission has a globally negative slope when $B_{*\mathrm{O}} = 100\,\mathrm{G}$, while the curves for lower values of $B_{*\mathrm{O}}$ do not. This arises because of the very steep particle distributions that are obtained when $B_{*\mathrm{O}} = 100\,\mathrm{G}$ (the standard case) due to the low values of S_{tot} and S_{sub} (see Fig. 6). As $B_{*\mathrm{O}}$ decreases and S_{tot} and S_{sub} increase, the IC emission attains a globally positive slope.

3.3.2 Radial stellar magnetic fields

We now explore how the particle acceleration and emission changes if we assume that the stars do not rotate. This results in a radial magnetic field in each stellar wind, which declines as r^{-2} (instead of a toroidal field that declines as r^{-1}). Hence this change affects both the strength of the pre-shock magnetic field, and its orientation to the shock. On the WCR axis the shocks become parallel (compared to almost perpendicular in the standard model).

Fig. 12 shows the pre-shock quantities as a function of the angle θ from the secondary star for the WR and O winds. Because the magnetic field in each stellar wind is now radial, and drops as r^{-2}, the pre-shock magnetic flux density is considerably lower than in the standard model, especially for the WR-shock. This results in both shocks becoming highly super-Alfvénic ($M_{\mathrm{A0x}} > 10^4$ for the WR-shock, and $M_{\mathrm{A0x}} \sim 10^3$ for the O-shock). Both shocks are parallel on-axis and become nearly perpendicular far off-axis. The reduced magnetic field strength also lowers the maximum momentum that the non-thermal protons attain (again, particularly for the WR-shock).

Fig. 13 shows the post-shock quantities as a function of the angle θ from the secondary star. Both the WR-shock and O-shock are now extremely efficient particle accelerators, and very high compression ratios are obtained. The latter occurs despite creation of non-negligible magnetic turbulence at the shock because of the very low magnetic field strength upstream. On axis the WR-shock puts 12 and 87 per cent of the incoming kinetic flux into non-thermal particles that flow downstream and escape upstream, respectively. For the O-shock these numbers are 32 and 65 per cent. The thermal X-ray emission from the WCR (not calculated) will be much softer from this model than the terminal speeds of the winds would suggest, because of the significantly lower post-shock temperatures that are obtained (as a large part of the input mechanical energy is used for particle acceleration). The turbulent magnetic field component
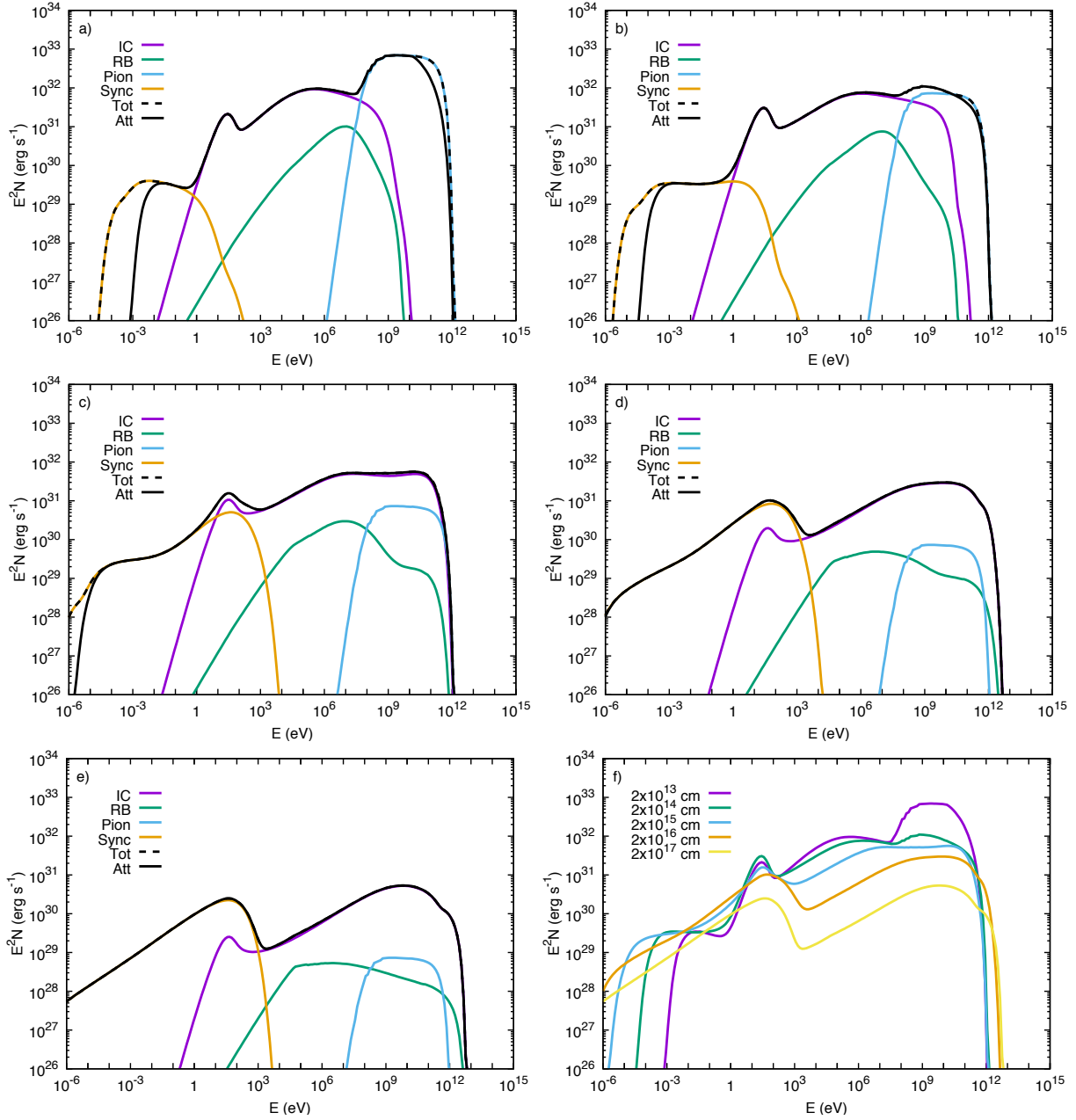
Figure 10. The dependence of the non-thermal emission on the stellar separation, D, which varies between each panel: a) $D = 2 \times 10^{13}$ cm; b) $D = 2 \times 10^{14}$ cm; c) $D = 2 \times 10^{15}$ cm; d) $D = 2 \times 10^{16}$ cm; e) $D = 2 \times 10^{17}$ cm. All other parameters are unchanged. In panel f) the total attenuated emission from each of these models is plotted. In all cases $\phi = 90°$.

dominates the uniform field component, for both shocks and in all locations, by more than an order of magnitude.

Another big change is the dramatic reduction in the maximum Lorentz factor of the non-thermal electrons. We see that $\gamma_{\mathrm{max,e}}$ drops from $\sim 10^6$ with a toroidal stellar magnetic field (see Fig. 2f) to $\sim 10^3$ when the field is radial. This is due to several factors: i) the large reduction in the flow speed immediately prior to the subshock (due to the large compression in the subshock in this model, $u_1 = u_0 R_{\mathrm{sub}}/R_{\mathrm{tot}} = 92 \, \mathrm{km \, s^{-1}}$, compared to $1700 \, \mathrm{km \, s^{-1}}$ in the standard model); ii) the low value of the magnetic field immediately prior to the subshock ($B_1 = 2.6 \times 10^{-5}$ G in this model, compared to 5×10^{-3} G in the standard model); iii) the strongly turbulent post-shock magnetic field ($B_{2,\mathrm{tot}} = 0.044$ in this model, versus 0.02 in the

standard model). Factors i) and ii) strongly reduce the acceleration rate of the electrons (cf. Eq. 5), by about a factor of 10^5, while iii) increases the synchrotron loss rate by a factor of ≈ 5.

Fig. 14 shows the on-axis particle distributions immediately downstream of the subshock. The strong concave curvature to the distributions indicates the significant modification of the shocks. The O-shock now contributes similarly to the non-thermal particle population, whereas in the standard model the O-shock contributed very little (cf. Fig. 6). Neither shock accelerates particles to particularly high energies, and as we have seen the electron maximum energy is considerably reduced. The thermal peak shows a significant shift to lower momenta, particularly for the WR-shock, indicating the considerable reduction in post-shock temperature.
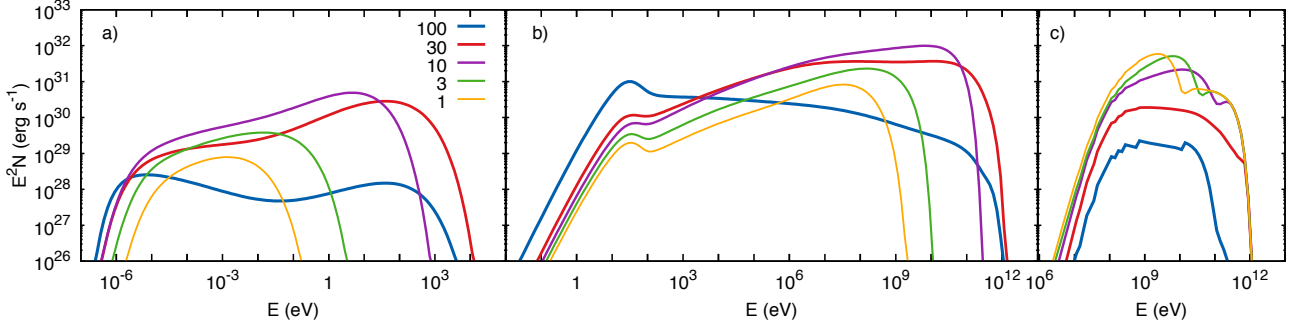
Figure 11. The intrinsic non-thermal emission from the particles accelerated at the O-shock when the surface magnetic field of the O-star is varied. a) The synchrotron emission. b) The inverse Compton emission. c) The emission from π^0-decay.

Figure 12. As Fig. 1 but for a model where the stars are not rotating, resulting in a radial magnetic field in each wind. All quantities are now independent of Φ.
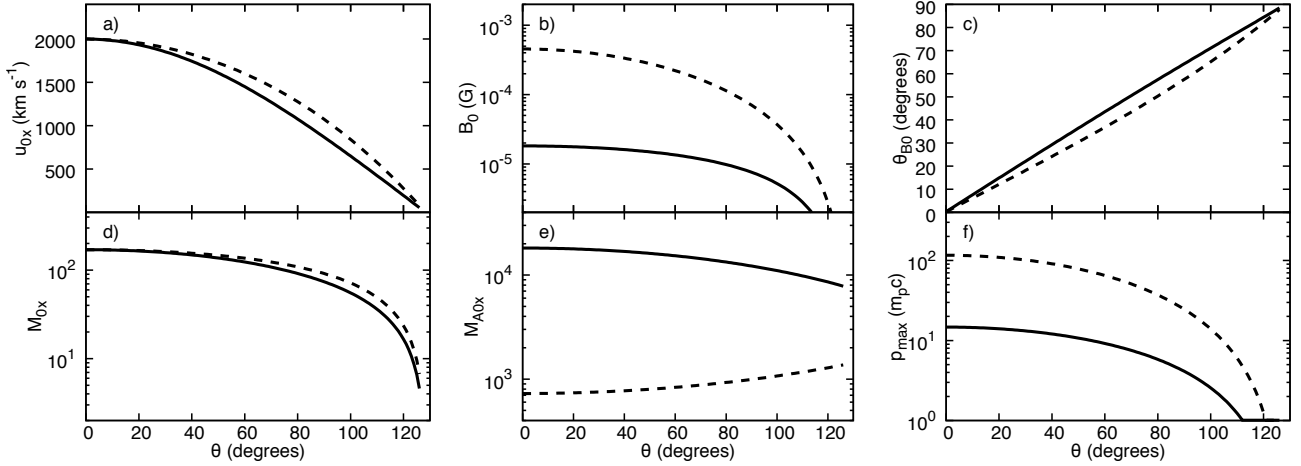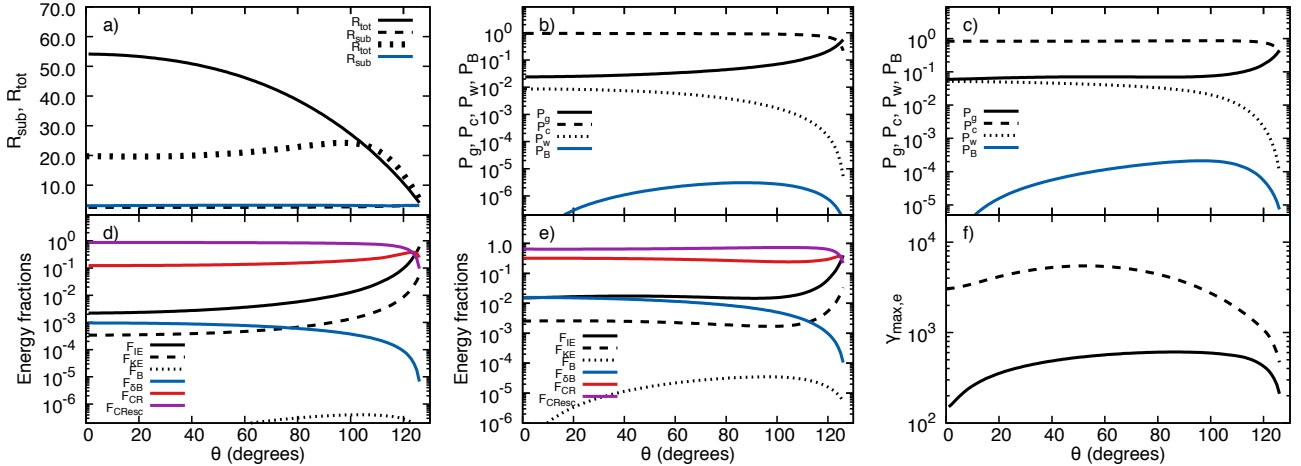

Figure 13. As Fig. 2 but for a model where the stars are not rotating, resulting in a radial magnetic field in each wind. All quantities are now independent of Φ.

In Fig. 15 we show the non-thermal emission from this model. The differences in the non-thermal particle distributions compared to the standard model result in significant differences to the non-thermal emission. First, we see a dramatic dip in the emission between energies of $0.1 - 10$ eV. This is caused by the significantly lower energies attained by the non-thermal electrons, which causes a reduction in the number of energy decades that the synchrotron (and inverse Compton) emission extends over. Second, the synchrotron and in-

verse Compton emission are both significantly weaker. Third, the reduction in p_{max} also lowers the maximum energy of the π^0-decay emission. Finally, we see that the π^0-decay emission is significantly stronger compared to the standard model at the same separation. This is because of the much higher density of the post-shock gas due to the increased compression of the shocks, plus the much lower flow speed of this gas, which means that the ratio of the non-thermal proton cooling timescale to the flow timescale has much reduced.
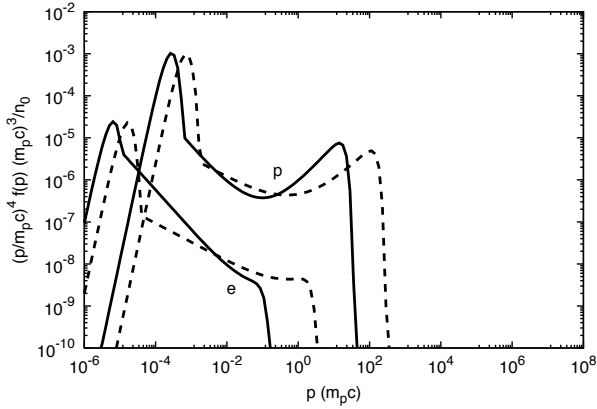
Figure 14. The proton and electron distributions for the WR-shock (solid line) and O-shock (dashed line) for $\theta = 0°$ when the magnetic field in each stellar wind is radial. The distributions are independent of Φ. For the WR-shock, $R_{tot} = S_{tot} = 54.1$ and $R_{sub} = S_{sub} = 2.5$. For the O-shock, $R_{tot} = 19.8$ and $R_{sub} = 3.09$, while $S_{tot} = 19.6$ and $S_{sub} = 3.06$. For both shocks $n_0 = 1.3 \times 10^5$ cm^{-3}. The thermal peaks are visible at low momenta. $D = 2 \times 10^{15}$ cm.
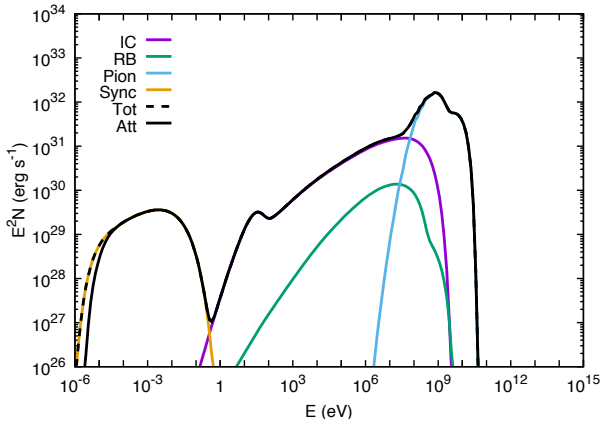

Figure 15. The non-thermal emission when the stellar rotation speeds are zero (in the standard model $v_{rot}/v_\infty = 0.1$). $D = 2 \times 10^{15}$ cm.

3.4 Secondary electron creation and emission

In some situations we might expect secondary electrons to make an important contribution to the overall emission. Secondary electrons can be created when non-thermal protons interact with either thermal protons or with photons. The former case is expected to be dominant in CWBs (see App. D). The emission from secondary electrons has the potential to dominate that from the primary electrons (those accelerated at the shocks) because the former originate from the non-thermal protons, which carry the majority of the energy that the non-thermal particles have (see, e.g., Orellana et al. 2007). It is also possible to create secondary electrons with higher maximum energies than the primary electrons (since the former is given by $0.05 E_{p,max}$, where $E_{p,max}$ is the maximum proton energy, while the latter depends on inverse Compton and synchrotron losses during shock acceleration). The secondary electrons have the same slope in their particle distribution as the primary protons.

In order for secondary electrons to dominate the emission the non-thermal protons must lose a significant fraction of their energy through collisions with thermal protons. The inelastic proton-proton cross-section is energy dependent, but we can take $\sigma_{pp} \approx 30$ mb as a

good approximation (see, e.g., Fig. A2 in Vila 2012, and also Eq. B6 in this work). The cooling rate of a non-thermal proton is then

$$\frac{1}{t_{pp}} \approx c n_p K_{pp} \sigma_{pp}, \qquad (8)$$

where n_p is the thermal proton number density and $K_{pp} \approx 0.5$ is the total inelasticity of the interaction.

For cooling to be effective we require $t_{pp} \lesssim t_{dyn} = D/v_{ps}$, where v_{ps} is the postshock flow speed. With $v_{ps} \sim v_\infty/R_{tot}$ and $n_p \sim R_{tot}\dot{M}/(4\pi D^2 v_\infty m_H)$, this gives

$$D \lesssim 10^{12} \frac{\dot{M}_{-5} R_{tot}^2}{v_{\infty,3}} \text{ cm}, \qquad (9)$$

where $\dot{M}_{-5} = \dot{M}/(10^{-5} \text{ M}_\odot \text{ yr}^{-1})$ and $v_{\infty,3} = v_\infty/(1000 \text{ km s}^{-1})$. For our standard model $\dot{M}_{-5} = 2$ and $v_{\infty,3} = 2$ for the primary star, and $R_{tot} \sim 4$, so secondary electrons should become important when $D_{sep} \lesssim 2 \times 10^{13}$ cm.

Fig. 16 compares the leptonic and total non-thermal emission arising from models that include or do not include secondary electrons. We see that the secondary electrons give a significant boost to the high energy inverse Compton emission (over the energy range $E = 10^5 - 10^{11}$ eV) and synchrotron emission (over the energy range $E = 10^{-3} - 10^4$ eV), and indeed emit at higher energies than the primary electrons are capable of. The emission produced by secondary electrons is aided by the fact that they are continually generated downstream (whereas the primary electrons cool as they flow downstream and so only have a short opportunity to create the highest energy synchrotron and inverse Compton emission).

Despite the significant boost to the leptonic emission that the secondaries provide, however, there is relatively little change in the spectrum of the total non-thermal emission. The reason is that at the energies where this boost to the emission occurs, other processes tend to be dominant (inverse Compton emission from the primary electrons masks the synchrotron emission from secondary electrons at $E \sim 10 - 10^3$ eV, and π^0-decay emission at $E \sim 10^8 - 10^{11}$ eV masks the inverse Compton emission from secondary electrons). Only between $10^5 - 10^8$ eV do the secondary electrons make a visible contribution to the total emission[6].

While secondary electrons do not appear to significantly affect the total non-thermal emission for the standard model parameters with $D \gtrsim 10^{13}$ cm, they may be more important in systems with higher stellar mass-loss rates and slower wind speeds, or if the primary protons are able to interact with dense, radiatively cooled, gas. White et al. (2020) show that secondary electrons dominate the emission between $E \approx 1 - 40$ MeV in their "off-periastron" models of η Carinae (see the top panel in their Fig. 3).

Secondary electrons can also become important in situations where the shocks are strongly modified and very high compression ratios are achieved. Fig. 17 compares the significance of secondary electrons in such models (see Fig. 13 for the R_{tot} values in this case). While secondary electrons only become important for stellar separations $D \lesssim 2 \times 10^{13}$ cm in models with the standard parameters, Fig. 17 shows that secondaries can become important at much wider stellar separations when the shocks are significantly modified. In this particular case they are starting to add significantly to the emission between $10^5 - 10^7$ eV.

---

[6] Note that the π^0-decay emission is the same in both models because cooling of the non-thermal protons is included in both - the difference is in whether the creation of secondary electrons is considered.
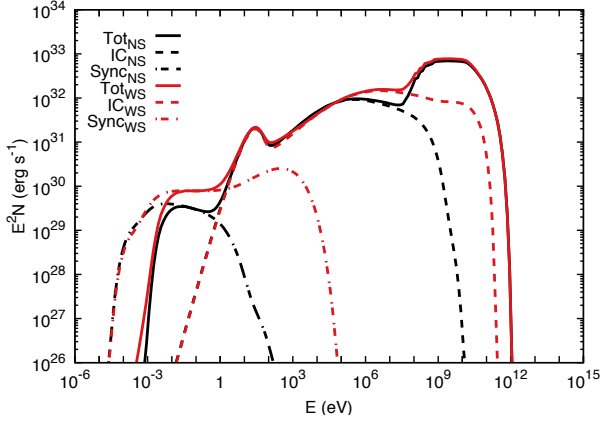
Figure 16. Comparison of the intrinsic non-thermal emission from models with (subscript WS; red lines) and without (subscript NS; black lines) secondary electrons ($D = 2 \times 10^{13}$ cm). The secondary electrons boost the inverse Compton and synchrotron emission.
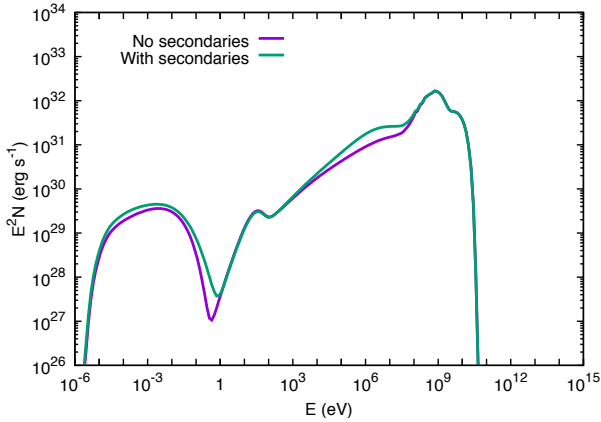

Figure 17. Comparison of the non-thermal emission from models with and without secondary electrons. $D = 2 \times 10^{15}$ cm and $v_{rot}/v_{\infty} = 0.0$ (i.e. the stellar winds have radial magnetic fields).

4 MODELLING THE RADIO EMISSION FROM WR 146

Having explored how the particle acceleration and non-thermal emission varies with stellar separation and the magnetic field in each wind, and the conditions under which secondary electrons become important, we now turn our attention to the modelling of a specific system. We choose WR 146, a WC6+O8I-IIf system (Lépine et al. 2001), because it is amongst the brightest CWBs at radio wavelengths and is also one of the few CWBs to be spatially resolved, with a southern thermal component and a northern non-thermal component (Dougherty et al. 1996, 2000; O'Connor et al. 2005). It has also been resolved at optical wavelengths by HST (Niemela et al. 1998), revealing a projected stellar separation of 168 ± 31 mas with the WR-star to the south and the O-star to the north. At 43 GHz there is a significant thermal contribution to the northern flux from the O-star wind (O'Connor et al. 2005). From the relative position of the components, O'Connor et al. (2005) inferred a wind momentum ratio of $\eta = 0.06 \pm 0.15$. More recently, a search for polarized radio emission has been made (Hales et al. 2017). WR 146 is currently the only CWB system to be detected at frequencies as low as 150 MHz (Benaglia et al. 2020). The distance to WR 146 is estimated as 1.2 ± 0.3 kpc (Dougherty et al. 1996), which is compatible with the *Gaia* DR2

estimate of $1.10^{+0.67}_{-0.36}$ kpc (Rate & Crowther 2020). At a distance of 1.2 kpc, the projected stellar separation is 2.9×10^{15} cm. Secondary electrons are not expected to be important in this system (see Eq. 9), and are therefore not included in the following models.

In their X-ray analysis of WR 146, Zhekov (2017) found that the predicted theoretical X-ray flux from their models far exceeded the observed emission. To bring the two measurements together required either substantially reducing their adopted mass-loss rates (by a factor of 10), or increasing the stellar separation D (by a factor of 66). The necessary change required for each variable in isolation is rather implausible, which suggests that they need to vary in combination, though even then the size of the required changes is rather overwhelming. One then wonders what other process could be at play. Zhekov (2017) note that models where the post-shock electrons are not in temperature equilibration with the ions can reduce the X-ray luminosity by another factor of two.

There seem to be three possible solutions to this problem. First, the wind momentum ratio may be too high (Zhekov (2017) assumed that $\eta = 0.11$). A lower value would mean that a smaller fraction of the WR wind is shocked, and since $L_x \propto \eta$ (Pittard & Dawson 2018), this would move the theoretical prediction towards the observed flux. However, given the magnitude of the excess emission this alone will not be enough. A second solution, which is not incompatible with the previous one, is that a significant fraction of the kinetic power of the stellar winds goes into non-thermal particles via DSA. Both of these possibilities are investigated below. Finally, a third possibility is that the post-shock flow is also not in ionization equilibrium. This may impact the X-ray luminosity but a detailed study is needed to determine at what level.

Our spectral models of WR 146 are constrained by the observed flux from this system. In the radio band we use the flux measurements by Hales et al. (2017) and Benaglia et al. (2020). We also include measurements obtained using the VLA in combination with the VLBA Pie Town antenna (see Table 3). In the X-ray band we use the on-axis ACIS-I *Chandra* pointed observation (Obs ID 7426) taken on March 17th 2007 (PI Pittard). This observation was designed to search for signs of weak shock heating and shock modification. Finally, there are also upper limits from 2 years of data from the *Fermi* satellite (Werner et al. 2013)[7]. To date, only one CWB has been detected at TeV energies (η Carinae; H.E.S.S. collaboration 2020).

4.1 The modelling

As it is unlikely that the stars are not rotating we adopt $v_{rot}/v_{\infty} = 0.1$, which leads to a toroidal magnetic field in each wind. We first attempted to fit the observational data with the assumption that the system is viewed face-on ($D = 2.9 \times 10^{15}$ cm; $i = 0°$; $\phi = 90°$). We adopted somewhat lower mass-loss rates than usually found in the literature, given the findings by Zhekov (2017): $\dot{M}_{WR} = 2 \times 10^{-5}$ M$_\odot$ yr^{-1} and $\dot{M}_O = 2 \times 10^{-6}$ M$_\odot$ yr^{-1}. With the observed terminal wind speeds this gives a wind momentum ratio $\eta = 0.057$. However, it proved impossible to obtain a good match to the observed synchrotron emission while simultaneously matching the turnover frequency at $\nu \approx 450$ MHz. In particular we found that the Razin turnover frequency was always too high, and the synchrotron luminosity too low. The former could be reduced by

---

[7] Pshirkov (2016) do not detect WR 146 in nearly 7 years of *Fermi* data, so should have been able to provide upper limits roughly 2× lower. However, due to possible contamination from a complicated neighbourhood, they declined to provide upper limits.
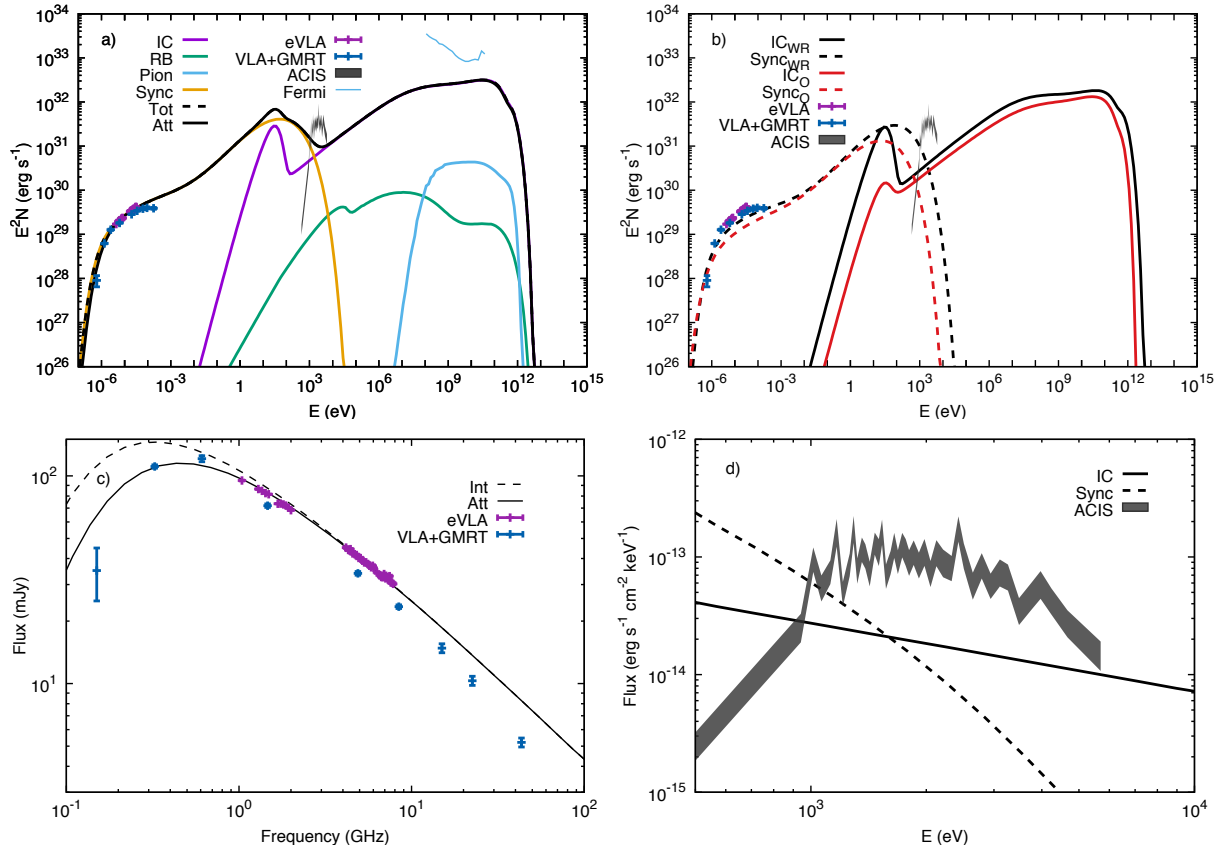
Figure 18. Model spectra for WR 146. a) The model inverse Compton, synchrotron, relativistic bremsstrahlung and π^0-decay emission are shown, together with the observed radio and thermal X-ray fluxes, and the upper limits from *Fermi*. b) The inverse Compton and synchrotron emission from particles accelerated at the WR-shock (black lines) and O-shock (red lines). c) The intrinsic and absorbed synchrotron radio emission from the model, and the observed radio emission. d) The observed X-ray emission and the non-thermal emission from the model. See Table 4 for the model parameters.

Table 3. Flux and RMS measurements of WR 146 obtained with the VLA in combination with the VLBA Pie Town antenna on October 1st 2004 (the 22 GHz data was obtained on November 8th 2004). Where two sources are resolved data is provided for both. At the lower frequencies where this is not the case all the flux is assigned to the northern source. From O'Connor et al. (2005).

Frequency (GHz)	N flux (mJy)	N RMS (mJy)	S flux (mJy)	S RMS (mJy)
1.465	71.92	1.4	0.0	0.0
4.885	33.96	0.68	0.0	0.0
8.435	23.46	0.47	0.0	0.0
15.00	14.82	0.74	3.59	0.18
22.46	10.33	0.52	5.17	0.26
43.34	5.21	0.26	6.59	0.33

reducing the stellar surface magnetic flux densities, but this led to lower synchrotron luminosity (cf. Fig. 11).

Since $\nu_R \approx 20\,n_e/B$, the Razin turnover frequency can be lowered in the case that $B \propto 1/D$ by increasing D. Increasing the stellar separation to $D = 1.2 \times 10^{16}$ cm ($i = 76°$; $\phi = 14°$) yielded ν_R at the correct frequency, but the synchrotron luminosity was still too low. To increase the synchrotron luminosity the O-star mass-loss rate was increased to $\dot{M}_O = 4 \times 10^{-6}$ M$_\odot$ yr^{-1}, giving a wind momentum ratio $\eta = 0.11$. This increase in η means that a greater

fraction of the WR-wind kinetic flux is intercepted by the WCR. The kinetic flux of the O-wind also doubles. The increase in $\dot{M}_O$ and η does indeed produce stronger synchrotron emission, and a reasonable match to the observational data is now obtained (see Fig. 18). With the assumed value of $v_{rot}/v_\infty = 0.1$ we require $B_{*WR} \approx 140$ G and $B_{*O} \approx 14$ G to match the turnover frequency and synchrotron flux. The turndown below 1 GHz is a combination of the Razin effect and free-free absorption (see Fig. 18c). The latter is sensitive to the volume filling factor of the clumps in the winds - here the winds are assumed to be smooth (i.e. $f = 1.0$; since the thermal free-free emission from the stellar winds is not calculated in our model, f only affects the free-free absorption through the O-wind in the current model). While our model is a good match to the recent eVLA data of Hales et al. (2017) and the GMRT data of Benaglia et al. (2020), it matches less well the derived fluxes from the older VLA + Pie Town data of O'Connor et al. (2005), which lie below the higher fluxes reported by Hales et al. (2017). The parameters of our model are noted in Table 4.

In our model the non-thermal particles accelerated at the WR-shock provide the majority of the emission, with the O-shock accelerated particles typically contributing about a third to the total flux. The WR-shock accelerated particles provide the highest energy inverse Compton and synchrotron emission (see Fig. 18b). The non-thermal X-ray flux predicted by the model is shown together with the observed X-ray emission in Fig. 18d). The inverse Compton emission barely drops below the observed thermal emission at $E \approx 6$ keV,

Table 4. The parameters used in our final model of WR 146. Our assumed $D = 1.2 \times 10^{16}$ cm implies that $i = 76°$ and $\phi = 14°$ (the O star is directly in front of the WR-star when $i = 90°$). The WR-star terminal wind speed is an average from Eenens & Williams (1994) and Willis et al. (1997). The O-star terminal wind speed is from the velocity ratio given in Dougherty et al. (2000). The O and WR-star luminosities are from O'Connor (private communication), and are estimated from Vacca, Garmany & Shull (1996) and the magnitude difference reported by Niemela et al. (1998). The hydrogen, helium and "metal" mass fractions are noted as X, Y and Z, respectively. The WR abundances are from Nugis & Lamers (2000).

Parameter	WR-star	O-star
$\dot{M}$ ($M_\odot\,yr^{-1}$)	2×10^{-5}	4×10^{-6}
v_∞ ($km\,s^{-1}$)	2800	1600
L ($L_\odot$)	2.3×10^5	7.9×10^5
T_{eff} (K)	49000	32000
R_* ($R_\odot$)	6.6	28.9
X	0.0	0.7381
Y	0.744	0.2485
Z	0.256	0.0134
B_* (G)	140	14
v_{rot}/v_∞	0.1	0.1
f	1.0	1.0

Table 5. The kinetic power of the winds, the kinetic flux at each shock, and the power put into non-thermal particles that are advected downstream or escape upstream from the shocks. All values are in $erg\,s^{-1}$.

Parameter	WR	O	Total
Wind kinetic power	5.0×10^{37}	3.3×10^{36}	5.3×10^{37}
Input power at shock	1.6×10^{36}	8.9×10^{35}	2.5×10^{36}
CR advection power	3.4×10^{35}	2.4×10^{35}	5.7×10^{35}
CR escape power	6.7×10^{34}	6.9×10^{34}	1.4×10^{35}

while the predicted synchrotron emission exceeds the observed thermal emission at $E < 1$ keV (note that no photoelectric absorption has been applied to the model emission). In our model the synchrotron flux at keV energies is sensitive to the value adopted for α in Eq. 4 and the assumption that the synchrotron loss rate at the shock depends on $B_{2,tot}$ (this latter assumption affects $p_{max,e}$). Both of these "close encounters" with the thermal X-ray emission may prove challenging to future models. In theory, they may allow tight constraints to be placed on the O-star luminosity (a higher luminosity would possibly decrease the maximum energy of the non-thermal electrons and thus the maximum energy that the synchrotron emission attains, but then would increase the predicted inverse Compton emission, while a lower luminosity would increase the maximum energy of the synchrotron emission). Future models should also investigate whether radial magnetic fields in the stellar winds produce a better match to the observations.

On axis the shocks put ≈ 20 per cent of the wind kinetic flux into non-thermal particles, while a further 5 per cent goes into non-thermal particles that escape upstream. Compression ratios of 4.7 are obtained. The upstream magnetic field strength is 0.72 and 0.93 mG for the WR and O-shock respectively, while the post-shock values are 3.4 and 4.3 mG.

Table 5 notes the kinetic power of each wind, the power available at each shock, and the power put into non-thermal particles that are advected downstream or escape upstream of each shock. The total power put into non-thermal particles is $7.1 \times 10^{35}\,erg\,s^{-1}$, which

represents an overall efficiency of conversion of the power available at the shocks of 29 per cent. Just over 1 per cent of the combined wind power of the stars goes into non-thermal particles.

4.2 Discussion

Compared to the model in Zhekov (2017), $\dot{M}_{WR}$ is 1.6 times lower, D is 3.5 times higher, and η is the same. Since the thermal X-ray luminosity for an adiabatic system scales as $L_x \propto \dot{M}^2 \eta D^{-1}$ (Stevens et al. 1992; Pittard & Dawson 2018), our model should be 9 times fainter by this measure. However, as 30 per cent of the available wind power is put into cosmic rays rather than thermalised gas, it should be ≈ 13 times fainter overall. Unfortunately, this is still less than the factor of $30 - 50$ reduction that Zhekov (2017) states is required if $T_e \leq T_{ion}$. Perhaps non-equilibrium ionization also has a role to play.

Turning our attention to the radio we note that although synchrotron emission is intrinsically polarized, Hales et al. (2017) found the fractional linear polarization from the radio synchrotron emission from WR 146 to be less than 0.6 per cent. The lack of polarization is naturally explained if the magnetic field is turbulent, and they estimate that the field has a dominant random component with $\delta B/B > 8$. In contrast, we find that the emission weighted value of $\delta B/B$ from our model is ≈ 2.4 at frequencies of $1 - 8$ GHz. This suggests that some other process or mechanism may be responsible for the lack of polarisation (see Hales et al. (2017) for a discussion of this). Alternatively, it may indicate that our models of WR 146 should have a magnetic field that is more turbulent. This is achieved in our model with radial magnetic fields in the stellar winds (see Sec. 3.3.2), where the turbulent component dominates for both shocks in all locations by more than an order of magnitude. The level of turbulence is interesting not least because a high level of turbulence may lead to ultra-fast acceleration in CWBs (and maximum energies above a few TeV), in contrast to SNRs which appear to accelerate particles close to the Bohm limit (Stage et al. 2006).

While we have indicated the simple fitting that we have attempted, we have certainly not exhausted all possibilities, and it is quite likely that fits as least as good will be found with other model parameters. This is because various trade-offs exist between the model parameters. For instance, increasing D generally leads to a drop in emission, but this can be offset by increasing $\dot{M}$. In addition, B_* and v_{rot}/v_∞ can be directly played off against each other. Having said this, the model does place some constraints. Too high values for the magnetic flux density result in particle distributions that are too steep. Too low values for B result in no or very weak acceleration, and/or too low values of p_{max} and $p_{max,e}$. A more detailed investigation, that will also model the free-free radio emission, the thermal X-ray emission, and produce radio images, is left to future work.

5 SUMMARY AND CONCLUSIONS

We report on the first particle acceleration model of colliding wind binaries that applies a non-linear diffusive shock acceleration model, with magnetic field amplification and relative motion of the scattering centres, to oblique shocks. We find that:

(i) The relative motion of the scattering centres with respect to the fluid can be significant. When this occurs we obtain steeper non-thermal particle distributions.

(ii) The particle acceleration is strongly dependent on the pre-shock magnetic field, and its efficiency can vary strongly along and between each shock.

(iii) The particle acceleration efficiency and non-thermal emission can behave non-linearly with the magnetic field strength at the shock. As the pre-shock magnetic flux density decreases, an increase in acceleration efficiency due to the increasing Alfvénic Mach number competes against a reduction in the maximum energy of the accelerated particles. This can result in the non-thermal emission peaking at intermediate values of the magnetic field strength.

(iv) The strength and angle to the shock normal of the pre-shock magnetic field depends strongly on whether the stellar winds have a toroidal field (i.e. the stars are rotating) or a radial field (i.e. the stars are non-rotating).

(v) The non-thermal emission may be dominated by particles accelerated by one or the other shock, or may be roughly equally split between both shocks.

(vi) The shock precursors are typically smaller than the scale of the WCR.

(vii) Downstream of the shock the dominant pressure may be from the gas or from the cosmic rays.

(viii) In some locations along the shocks we find that $\delta B > B$, while the opposite is true in other locations. In our standard model we find that the WR-shock is largely turbulent while the O-shock is not. Whether or not a shock is turbulent depends sensitively on the model parameters, such as the strength of the surface magnetic field and rotation speed of the star. In some systems the synchrotron emission should not be significantly polarized, while in others it may be.

(ix) Local particle acceleration efficiencies for the downstream flowing cosmic rays of up to 30 per cent are obtained. Such values can arise when the shocks are perpendicular, oblique, or parallel. When the magnetic field in the stellar wind is radial, the lower pre-shock magnetic flux densities that result mean that up to nearly 90 per cent of the local kinetic flux may go into cosmic rays that escape upstream. Under other conditions the advected and escape cosmic ray energy fractions may be much reduced.

(x) The gas compression ranges from ≤ 4 to over 20 in some cases. High ratios have a significant effect on the strength of the emission from π^0-decay and secondary electrons, and will also affect the postshock temperature and the thermal X-ray emission.

Given the large variation in the spectral indices of the non-thermal particles seen in our models, it is clearly necessary to go beyond the assumption that $f(p) \propto p^{-4}$ (equivalent to $N(E) \propto E^{-2}$). While previous works have varied the spectral index of the non-thermal particles as a model *input* (e.g., Pittard et al. 2006; Pittard & Dougherty 2006; del Palacio et al. 2016, 2020), our new model produces the spectral index as an *output*, and allows it to vary along and between the shocks, and as a function of energy or momentum. We draw attention to the fact that the values of the energy index output from our standard model corresponds precisely to the indices adopted by del Palacio et al. (2016, 2020) to match the observed emission from HD 93129A.

We also derive an analytical expression to determine when emission from secondary electrons is expected to make an important contribution to the total emission (Eq. 9). Such secondaries can produce emission at higher energy than the primary electrons, but we also show how the additional emission can sometimes be masked by other emission processes.

Our new model has been applied to WR 146, one of the brightest CWB systems in the radio band. We are able to obtain a good match to the radio flux, reproducing both the curvature of the eVLA data plus the low frequency turnover. Our model is also consistent with other data: the non-thermal emission is fainter than the observed thermal

X-ray emission and the *Fermi* upperlimit. The model converts ≈ 30 per cent of the kinetic wind power at the shocks into non-thermal particles. If this WR+O system has a lifetime of $\approx 3 \times 10^5$ yr, it will put nearly 10^{49} erg into non-thermal particles during this evolutionary phase of the stars. Significant energy may also go into cosmic rays during the prior O+O phase which involves weaker winds but is longer lasting.

DATA AVAILABILITY

The data underlying this article are available in the Research Data Leed Repository, at https://doi.org/XXX.

REFERENCES

Amato E., Blasi P., 2005, MNRAS, 364, L76
Amato E., Blasi P., 2006, MNRAS, 371, 1251
Atoyan A.M., Dermer C.D., 2003, ApJ, 586, 79
Bednarek W., 2005, MNRAS, 363, L46
Bell A.R., 1978, MNRAS, 182, 147
Bell A.R., Schure K.M., Reville B., Giacinti G., 2013, MNRAS, 431, 415
Benaglia P., De Becker M., Ishwara-Chandra C.H., Intema H., Isequilla N.L., 2020, PASA, 37, 30
Benaglia P., Marcote B., Moldón J., Nelan E., De Becker M., Dougherty S.M., Koribalski B.S., 2015, A&A, 579, A99
Blasi P., 2002, Astropart. Phys., 16, 429
Blasi P., Gabici S., Vannoni G., 2005, MNRAS, 361, 907
Blasi P., Amato E., Caprioli D., 2007, MNRAS, 375, 1471
Blomme R., et al., 2013, A&A, 550, A90
Blomme R., Fenech D.M., Prinja R.K., Pittard J.M., Morford J.C., 2017, A&A, 608, A69
Blumenthal G.R., Gould R.J., 1970, Rev. Mod. Phys., 42, 237
Brookes D.P., 2016, PhD thesis, The University of Birmingham
Bykov A.M., Ellison D.C., Osipov S.M., Vladimirov A.E., 2014, ApJ, 789, 137
Cantó J., Raga A.C., Wilkin F.P., 1996, ApJ, 469, 729
Caprioli D., Blasi P., Amato E., Vietri M., 2009, MNRAS, 395, 895
Caprioli D., Kang H., Vladimirov A.E., Jones T.W., 2010, MNRAS, 407, 1773
Caprioli D., Pop A.-R., Spitovsky A., 2015, ApJL, 798, L28
Caprioli D., Spitovsky A., 2014, ApJ, 783, 91
Caprioli D., Zhang H., Spitovsky A., 2018, Journal of Plasma Physics, 84, 715840301
Corcoran M.F., Hamaguchi K., Pittard J.M., Russell C.M.P., Owocki S.P., Parkin E.R., Okazaki A., 2010, ApJ, 725, 1528
De Becker M., Benaglia P., Romero G.E., Peri C.S., 2017, A&A, 600, A47
De Becker M., Raucq F., 2013, A&A, 558, A28
Decker R.B., 1988, Space Sci. Rev., 48, 195
del Palacio S., Bosch-Ramon V., Romero G., Benaglia P., 2016, A&A, 591, 139

del Palacio S., et al., 2020, MNRAS, 494, 6043

Dougherty S.M., Beasley A.J., Claussen M.J., Zauderer B.A., Bolingbroke N.J., 2005, ApJ, 623, 447

Dougherty S.M., Pittard J.M., Kasian L., Coker R.F., Williams P.M., Lloyd H.M., 2003, A&A, 409, 217

Dougherty S.M., Pittard J.M., 2006, in Proc. of the 8th European VLBI Network Symp., 49

Dougherty S.M., Williams P.M., Pollacco D.L., 2000, MNRAS, 316, 143

Dougherty S.M., Williams P.M., van der Hucht K.A., Bode M.F., Davis R.J., 1996, MNRAS, 280, 963

Dubus G., 2006, A&A, 451, 9

Eenens P.R.J., Williams P.M., 1994, MNRAS, 269, 1082

Eichler D., Usov V., 1993, ApJ, 402, 271

Ellison D.C., Decourchelle A., Ballet J., 2004, A&A, 413, 189

García-Segura G., 1997, ApJ, 489, L189

Giacalone J., 2005, ApJ, 624, 765

Ginzburg V., Syrovatskii S., 1964, "The Origin of Cosmic Rays" (New York: Macmillan)

Ginzburg V., Syrovatskii S., 1965, ARA&A, 3, 297

Gould R.J., Schréder G.P., 1967, Phys. Rev., 155, 1404

Grevesse N., Asplund M., Sauval A.J., Scott P., 2010, Astrophys. Space Sci., 328, 179

Grimaldo E., Reimer A., Kissmann R., Niederwanger F., Reitberger K., 2019, ApJ, 871, 55

Haggerty C.C., Caprioli D., 2019, ApJ, 887, 165

Hales C.A., Benaglia P., del Palacio S., Romero G.E., Koribalski B.S., 2017, A&A, 598, A42

Hamaguchi K., et al., 2007, ApJ, 663, 522

Hamaguchi K., et al., 2014a, ApJ, 784, 125

Hamaguchi K., et al., 2014b, ApJ, 795, 119

Hamaguchi K., et al., 2016, ApJ, 817, 23

Hamaguchi K., et al., 2018, Nature Astronomy, 2, 731

Henley D. B., Corcoran M. F., Pittard J. M., Stevens I. R., Hamaguchi K., Gull T. R., 2008, ApJ, 680, 705

H.E.S.S. Collaboration, Abdalla et al., 2020, A&A, 635, A167

Hillas A.M., 1984, ARA&A, 22, 425

Hussein M., Shalchi A., 2014, ApJ, 785, 31

Jones F.C., Ellison D.C., 1991, Space Sci. Rev., 58, 259

Kato T.N., 2015, ApJ, 802, 115

Khangulyan D., Aharonian F.A., Bosch-Ramon V., 2008, MNRAS, 383, 467

Khangulyan D., Aharonian F.A., Kelner S.R., 2014, ApJ, 783, 100

Kelner S.R., Aharonian F.A., Bugayov V.V., 2006, Phys. Rev. D, 74, 034018

Kelner S.R., Aharonian F.A., 2008, Phys. Rev. D, 78, 034013

Lagage P.O, Cesarsky C.J., 1983, A&A, 125, 249

Lépine S., Wallace D., Shara M.M., Moffat A.F.J., Niemela V.S., 2001, AJ, 122, 3407

Longair M.S., 1994, High Energy Astrophysics. Vol. 2, 2nd edn., Cambridge Univ. Press, Cambridge

Mannheim K., Schlickeiser R., 1994, A&A, 286, 983

Mahadevan R., Narayan R., Yi I., 1996, ApJ, 465, 327

Melrose D.B., 1980, Plasma astrophysics: Nonthermal processes in diffuse magnetized plasmas, Astrophysical applications (New York, Gordon and Breach Science Publishers), 2, 430

Möller T., Trumbore B., 1997, Journal of Graphics Tools, 2, 21

Morlino G., Caprioli D., 2012, A&A, 538, A81

Mücke A., Engel R., Rachen J.P., Protheroe R.J., Stanev T., 2000, Comput. Phys. Commun., 124, 290

Nakamura K., et al., 2010, J. Phys. G Nucl. Partic., 37, 075021

Niemela V.S., Shara M.M., Wallace D.J., Zurek D.R., Moffat A.F.J., 1998, AJ, 115, 2047

Nugis T., Lamers H.J.G.L.M., 2000, A&A, 360, 227

O'Connor E.P., Dougherty S.M., Pittard J.M., Williams P.M., 2005, in Massive Stars and High-Energy Emission in OB Associations, eds. G. Rauw, Y. Nazé, R. Blomme, & E. Gosset, 81

Orellana M., Bordas P., Bosch-Ramon V., Romero G., Paredes J.M., 2007, A&A, 476, 9

Ortiz-León G., Loinard L., Rodríguez L.F., Mioduszewski A.J., Dzib S.A., 2011, ApJ, 737, 30

Panagia N., Felli M., 1975, A&A, 39, 1

Park J., Caprioli D., Spitkovsky A., 2015, Phys. Rev. Lett., 114, 085003

Parkin E. R., Gosset E., 2011, A&A, 530, A119

Parkin E. R., Pittard J.M., 2008, MNRAS, 388, 1047

Parkin E. R., Pittard J. M., Corcoran M. F., Hamaguchi K., 2011, ApJ, 726, 105

Parkin E. R., Pittard J. M., Nazé Y., Blomme R., 2014, A&A, 570, A10

Pittard J.M., 2009, MNRAS, 396, 1743

Pittard J.M., Dawson B., 2018, MNRAS, 477, 5640

Pittard J.M., Dougherty S.M., 2006, MNRAS, 372, 801

Pittard J.M., Dougherty S.M., Coker R.F., O'Connor E., Bolingbroke N.J., 2006, A&A, 446, 1001

Pittard J.M., Parkin E.R., 2010, MNRAS, 403, 1657

Pittard J.M., Vila G.S., Romero G.E., 2020, MNRAS, 495, 2205

Pollock A. M. T., Corcoran M. F., Stevens I. R., Williams P. M., 2005, ApJ, 629, 482

Pshirkov M.S., 2016, MNRAS, 457, L99

Rate G., Crowther P.A., 2020, MNRAS, 493, 1512

Razin V.A., 1960, Radiophysica, 3, 584

Reitberger K., Reimer A., Reimer O., Takahashi H., 2015, A&A, 577, A100

Reville B., Bell A.R., 2013, MNRAS, 430, 2873

Romero G.E., del Valle M.V., Orellana M., 2010, A&A, 518, A12

Schlick C., Subrenat G., 1993, "Ray Intersection of Tessellated Surfaces: Quadrangles versus Triangles", Graphics Gems V, Academic Press, p232

Stage M.D., Allen G.E., Houck J.C., Davis J.E., 2006, Nature Physics, 2, 614

Stevens I.R., Blondin J.M., Pollock A.M.T., 1992, ApJ, 386, 265

Sugawara Y., et al., 2015, PASJ, 67, 121

Tsytovitch V.N., 1951, Vest. Mosk. Univ., 11, 27

Vacca W.D., Garmany C.D., Shull J.M., 1996, ApJ, 460, 914

Van Loo S., Runacres M.C., Blomme R., 2004, A&A, 418, 717

van Marle A.J., Casse F., Marcowith A., 2018, MNRAS, 473, 3394

Vainio R., Schlickeiser R., 1999, A&A, 343, 303

Vila G.S., 2012, PhD thesis "Radiative models for jets in X-ray binaries", Universidad de Buenos Aires

Werner M., Reimer O., Reimer A., Egberts K., 2013, A&A, 555, A102

White R., Breuhaus M., Konno R., Ohm S., Reville B., Hinton J.A., 2020, A&A, 635, A144

Williams P.M., Dougherty S.M., Davis R.J., van der Hucht K.A., Bode M.F., Setia Gunawan D.Y.A., 1997, MNRAS, 289, 10

Willis A.J., Dessart L., Crowther P.A., Morris P.W., van der Hucht K.A., 1997, Ap&SS, 255, 167

Wright A.E., Barlow M.J., 1975, MNRAS, 170, 41

Xu R., Spitkovsky A., Caprioli D., 2020, ApJL, 897, L41

Zhekov S.A., 2017, MNRAS, 472, 4374

APPENDIX A: SEMIANALYTICAL NONLINEAR CALCULATION OF PARTICLE ACCELERATION

In this appendix we provide equations and the method for obtaining an exact solution for the spatial and momentum distribution of particles accelerated at a shock. The non-thermal particles generate Alfvén waves, and the magnetic turbulence and the cosmic rays dynamically react back on the shock. The method is based on a 1D kinetic treatment of parallel shocks developed by Amato & Blasi (2005, 2006) and Caprioli et al. (2009), and modified by Grimaldo et al. (2019) to include a pressure term from a transverse component of the background magnetic field. Like Grimaldo et al. (2019) we do not consider how the DSA efficiency changes with the obliquity of the shock - this possibility is discussed further in Sec. 2.2.1. We assume that all quantities change locally only in the x-direction which is perpendicular to the shock and that the magnetic field lies in the x-z plane. Unlike Grimaldo et al. (2019), we assume that the scattering centres move relative to the fluid at the Alfvén velocity.

The solution is obtained by iteratively solving the diffusion-advection equation for the shock-accelerated particles. The cosmic

rays are described by their distribution function in phase space $f(x, p)$ where p is the particle momentum. Keeping only the isotropic part, the diffusion-advection equation for a 1D non-relativistic shock is:

$$[u_x(x) - v_A(x)] \frac{\partial f(x,p)}{\partial x} = \frac{\partial}{\partial x} \left[D(x,p) \frac{\partial}{\partial x} f(x,p) \right]$$
$$+ \frac{d[u_x(x) - v_A(x)]}{dx} \frac{p}{3} \frac{\partial f(x,p)}{\partial p} + Q(x,p), \quad \text{(A1)}$$

where $u_x(x)$ is the flow speed in the x-direction, $v_A(x)$ is the Alfvén velocity, $D(x, p)$ is the diffusion coefficient, and $Q(x, p)$ describes the injection of particles into the acceleration process. The calculation is performed in the frame of the sub-shock which is located at $x = 0$; upstream is at $x < 0$ and downstream is at $x > 0$. In the following, quantities evaluated far upstream are given the prefix "0", quantities evaluated immediately upstream of the subshock are given the prefix "1", and quantities evaluated immediately downstream of the subshock are given the prefix "2".

The input values are the conditions far upstream: the flow density, ρ_0, the flow velocity in the x-direction, u_{0x}, the gas thermal pressure, p_{g0}, the flux density of the unperturbed magnetic field, B_0, and the angle it makes to the shock normal, θ_{B0}. In the following, velocities and pressures indicated with capital letters are normalized by u_{0x} and $\rho_0 u_{0x}^2$, respectively.

We consider only Alfvén waves generated by the resonant-streaming instability. The local Alfvén velocity is given by

$$v_A(x) = \frac{B(x)}{\sqrt{4\pi\rho(x)}}, \quad \text{(A2)}$$

where $\rho(x)$ and $B(x)$ are the local gas density and magnetic flux density of the uniform field, respectively. B_x is constant throughout the shock, while B_z changes in the shock precursor and across the subshock. Hence θ_B is also a function of x.

We suppose that the diffusion coefficient is given by Bohm diffusion[8] in the self-generated magnetic field (e.g., Jones & Ellison 1991) so that

$$\begin{aligned} D(x,p) &= D_\parallel(x,p)\cos^2\theta_B(x) + D_\perp(x,p)\sin^2\theta_B(x), \\ D_\parallel(x,p) &= \frac{pc}{eB(x)}\frac{c}{3}, \\ D_\perp(x,p) &= \frac{1}{4}\frac{pc}{eB(x)}\frac{c}{3}. \end{aligned} \quad \text{(A3)}$$

$D_\parallel$ and $D_\perp$ are the diffusion coefficients parallel and perpendicular to the magnetic field lines, respectively.

We assume that particle injection occurs only at the shock and for particles with momentum p_{inj}, such that

$$Q(x,p) = \eta \frac{\rho_1 u_{1x}}{4\pi m_p p_{inj}^2} \delta(p - p_{inj})\delta(x), \quad \text{(A4)}$$

where we adopt the recipe of Blasi, Gabici & Vannoni (2005) for the

[8] In Bohm diffusion the mean free path $l = r_L$, where $r_L = pc/(eB)$ is the Larmor radius. This results in a diffusion coefficient $D = r_L c/3$, which is reasonable for situations with $\delta B/B \sim 1$. However, when the turbulence is very strong, the particles experience very strong scattering and the mean-free path becomes $l = r_L B/\delta B$ (Hussein & Shalchi 2014). This results in a smaller diffusion coefficient and shorter acceleration timescales for the particles in the context of DSA. The maximum energy of particles may then be underestimated in the case of WR 146, where the absence of polarization suggests very strong turbulence.

fraction η of injected particles:

$$\eta = \frac{4}{3\sqrt{\pi}}(S_{sub} - 1)\chi^3 e^{-\chi^2}. \quad \text{(A5)}$$

This prescription assumes that only particles with momentum $p_{inj} \geq \chi p_{th,2}$ can be accelerated, where $p_{th,2}$ is the momentum of the thermal peak in the post shock gas. We follow Caprioli et al. (2009) and set $\chi = 3.75$ in all of our simulations.

A very good approximation for the solution of Eq. A1 is (Amato & Blasi 2005, 2006; Blasi et al. 2007)

$$f(x,p) = f_1(p)\exp\left[-\frac{(S_{sub} - 1)}{S_{sub}} \frac{q(p)u_0}{3} \int_{-\infty}^0 \frac{U_x(x') - V_A(x')}{D(x',p)} dx' \right], \quad \text{(A6)}$$

where $V_A(x) = v_A(x)/u_{0x}$, $f_1 = f(0, p)$ and $q(p) = -\frac{d\log f_1(p)}{d\log p}$ is the spectral slope at the shock location.

Blasi (2002) showed that $f_1(p)$ can be written as

$$f_1(p) = \left(\frac{3S_{tot}}{S_{tot}U_{px}(p) - 1} \right) \frac{\eta\rho_1}{4\pi m_p p_{inj}^3}$$
$$\times \exp\left[-\int_{p_{inj}}^p \frac{3S_{tot}U_{px}(p')}{S_{tot}U_{px}(p') - 1} \frac{dp'}{p'} \right], \quad \text{(A7)}$$

where

$$U_{px}(p) = U_{1x} - V_{A1} - \frac{1}{f_1(p)} \int_{-\infty}^0 f(x,p) \frac{d[U_x(x) - V_A(x)]}{dx} dx. \quad \text{(A8)}$$

$u_x(p) = U_{px}(p)u_{0x}$ is the mean velocity effectively felt by a particle with momentum p in the upstream region.

The method of solution is based also on the momentum flux conservation equation, normalized to $\rho_0 u_{0x}^2$:

$$U_x(x) + P_c(x) + P_w(x) + P_g(x) + P_B(x) = 1 + P_{g0} + P_{B0}, \quad \text{(A9)}$$

where the normalized thermal pressure $P_{g0} = 1/(\gamma M_{0x}^2)$ and $M_{0x}^2 = \rho_0 u_{0x}^2/(\gamma p_{g0})$. The normalized pressure in cosmic rays is

$$P_c(x) = \frac{4\pi}{3\rho_0 u_{0x}^2} \int_{p_{inj}}^\infty p^3 v(p)f(x,p) \, dp, \quad \text{(A10)}$$

where $v(p)$ is the velocity of a particle with momentum p, while the normalized pressure in magnetic turbulence generated via the resonant streaming instability is

$$P_w(x) = \frac{v_A(x)}{4u_{0x}} \frac{1 - U(x)^2}{U(x)^{3/2}} \cos\theta_{B0}. \quad \text{(A11)}$$

If the heating of the background gas, with adiabatic index γ, in the precursor is purely adiabatic, the normalized gas pressure is

$$P_g(x) = \frac{U_x(x)^{-\gamma}}{\gamma M_{0x}^2}. \quad \text{(A12)}$$

The z-component of the magnetic field exerts a normalized pressure

$$P_B(x) = \frac{B_z(x)^2}{8\pi\rho_0 u_{0x}^2}, \quad \text{(A13)}$$

where

$$B_z(x) = \left(\frac{M_{A0x}^2 - \cos^2\theta_{B0}}{U_x(x)M_{A0x}^2 - \cos^2\theta_{B0}} \right) B_{0z} \quad \text{(A14)}$$

and $M_{A0x} = u_{0x}/v_A$. If the shock is not strictly parallel P_B is present.

Given a value for $U_{1x} = R_{sub}/R_{tot}$, the normalized values P_{g1}, P_{w1}, P_{c1}, and P_{B1} are determined. R_{sub} can then be determined by solving the third-order equation (cf. Decker 1988; Vainio & Schlickeiser 1999; Grimaldo et al. 2019)[9]

$$a_3 R_{sub}^3 + a_2 R_{sub}^2 + a_1 R_{sub} + a_0 = 0, \tag{A15}$$

with coefficients

$$
\begin{aligned}
a_3 &= \left[(\gamma - 1)(1 + \lambda)M_{A1x}^2 + \gamma\beta_1 \cos^2\theta_{B1}\right]\cos^2\theta_{B1}, \\
a_2 &= \Bigg[\left[2(1 + \lambda) - \gamma(1 + \cos^2\theta_{B1} + \lambda)\right]M_{A1x}^2 \\
&\quad - \left[1 + \lambda + \gamma(2\beta_1 + 1 + \lambda)\right]\cos^2\theta_{B1}\Bigg]M_{A1x}^2, \\
a_1 &= \left[(\gamma - 1)M_{A1x}^2 + \gamma(1 + \lambda + \cos^2\theta_{B1} + \beta_1)\right. \tag{A16} \\
&\quad \left. + 2\cos^2\theta_{B1}\right]M_{A1x}^4, \\
a_0 &= -(\gamma + 1)M_{A1x}^6.
\end{aligned}
$$

In the above equations, $\lambda = (\delta B_1/B_1)^2$, $M_{A1x} = u_{1x}/v_A$, and β is the plamsa beta given by $\beta = 8\pi p_g/B^2$. This then yields a value for R_{tot}.

To solve these equations a numerical grid spanning $x/x_* = 10^{-10} - 100$, where $x_* = -D(p_{max})/u_{0x}$ and $D(p_{max})$ is calculated using p_{max}, B_{1x} and B_{1z}. A momentum grid spanning p_{inj} to p_{max} is also used. Each grid has 600 bins distributed logarithmically. The following solution method is used:

(i) For a given p_{max}, and upstream flow parameters ρ_0, u_{0x}, T_0, B_0 and θ_{B0}, guess an initial value of U_{1x}. Given U_{1x}, calculate P_{g1}, P_{w1}, P_{c1}, B_{1z} and P_{B1}.

(ii) Set $U_x(x) = U_{1x}$ for all x and $U_{px}(p) = U_{1x}$ for all p on the momentum grid. Set $P_g(x) = P_{g1}$, $P_B(x) = P_{B1}$, $P_w(x) = P_{w1}$ and $P_c(x) = P_{c1}$ for all x. Set $B_z(x) = B_{1z}$ for all x. Determine all immediate pre-shock quantities (with subscript 1).

(iii) Determine R_{sub}, R_{tot}, all immediate post-shock quantities (with subscript 2), S_{sub}, S_{tot}, p_{inj} and η. $B_{2x} = B_{1x}$ and $B_{2z} = R_{sub}B_{1z}$.

(iv) Calculate $\rho(x)$, $B(x)$ and $V_A(x)$ for all x. The magnetic flux density of the uniform field is given by $B(x) = \sqrt{B_x^2(x) + B_z^2(x)}$.

(v) Calculate $f_1(p)$.

(vi) Calculate P_c from $f_1(p)$ and compare to P_{c1}. Let $K = P_{c1}/P_c$. Renormalize $f_1(p)$ by multiplying by K.

(vii) If K is converged with its previous value goto item (xiii) below. Otherwise calculate $q(p)$, $D(x, p)$, $f(x, p)$, and $P_c(x)$.

(viii) Calculate $U_x(x)$ from Eq. A9. To achieve faster convergence average the flow profile $U_x(x)$ with its previous value.

(ix) Update $\rho(x)$, $P_g(x)$, $P_w(x)$, $B_z(x)$, $B(x)$, $P_B(x)$, and $V_A(x)$.

(x) Update the immediate pre-shock quantities from these values (e.g., $U_{1x} = U_x(x = 0^-)$ where $x = 0^-$ is immediately upstream of the subshock).

(xi) Determine R_{sub}, R_{tot}, all immediate post-shock quantities (with subscript 2), S_{sub}, S_{tot}, p_{inj} and η.

(xii) Update $U_{px}(p)$ and goto item (v) above.

(xiii) In general convergence will be achieved for $K \neq 1$. However, the correct solution is only obtained when $K = 1$, which will usually require restarting the calculation with a different initial value of U_1 (i.e. goto item (i) above). This can be driven by a standard numerical root-finding procedure.

---

[9] Note that Vainio & Schlickeiser (1999) use an incorrect definition for β, which misses out a factor of $2/\gamma$. In addition, Eq. 16 in Caprioli et al. (2009) for R_{sub} is incorrect.

The distribution function $f(x, p)$ so obtained is then a solution of both the transport and conservation equations.

The flux of non-thermal particles that escape upstream of the shock can be determined from the equation for the conservation of energy flux

$$\frac{1}{2}\rho_2 u_{2x}^3 + \frac{\gamma_g}{\gamma_g - 1}p_{g2}u_{2x} + \frac{\gamma_c}{\gamma_c - 1}p_{c2}u_{2x} + 3p_{w2}u_{2x} + \frac{B_2^2}{4\pi}u_{2x}$$

$$= \frac{1}{2}\rho_0 u_{0x}^3 + \frac{\gamma_g}{\gamma_g - 1}p_{g0}u_{0x} + \frac{B_0^2}{4\pi}u_{0x} - F_{CResc}, \tag{A17}$$

where F_{CResc} is the energy flux of particles escaping at the maximum momentum from the upstream section of the fluid.

APPENDIX B: CREATION OF SECONDARY PARTICLES AND γ-RAYS VIA PROTON-PROTON INTERACTIONS

In this appendix we provide equations for some of the emissivity calculations in our models (see Orellana et al. (2007) and Vila (2012) for further details).

Proton-proton inelastic collisions create pions through the following reactions:

$$
\begin{aligned}
p + p &\to p + p + a\pi^0 + b\left(\pi^+ + \pi^-\right) \\
p + p &\to p + n + \pi^+ + a\pi^0 + b\left(\pi^+ + \pi^-\right) \tag{B1} \\
p + p &\to n + n + 2\pi^+ + a\pi^0 + b\left(\pi^+ + \pi^-\right).
\end{aligned}
$$

The integers a and b are the pions multiplicities. They depend on the energy of the relativistic proton approximately as $a, b \propto E_p^{-\kappa}$ with $\kappa \sim 1/4$ (Mannheim & Schlickeiser 1994). The threshold energy for the production of a single neutral pion is

$$E_{thr} = m_p c^2 + 2m_{\pi^0}c^2\left(1 + \frac{m_{\pi^0}}{4m_p}\right) \approx 1.22\,\text{GeV}, \tag{B2}$$

where m_p and m_{π^0} are the mass of the proton and the neutral pion, respectively.

The decay of neutral pions into γ-rays is calculated as in Appendix A3 in Pittard et al. (2020). The main decay channels for the charged pions created in proton-proton inelastic collisions are:

$$
\begin{aligned}
\pi^+ &\to \mu^+ + \nu_\mu, \\
\pi^- &\to \mu^- + \overline{\nu}_\mu, \tag{B3}
\end{aligned}
$$

with a branching ratio of 99.98770 ± 0.00004 (Nakamura et al. 2010). Muons decay with a probability almost equal to unity into a neutrino, an antineutrino, and an electron/positron:

$$
\begin{aligned}
\mu^+ &\to e^+ + \nu_e + \overline{\nu}_\mu \tag{B4} \\
\mu^- &\to e^- + \overline{\nu}_e + \nu_\mu.
\end{aligned}
$$

The charged muons decay over very short distances compared to the size of the WCR, so the electron and positron are assumed to be injected "on-the-spot".

Kelner et al. (2006) provide simple analytical formulae for the cross-section and energy spectra of the products of inelastic proton-proton collisions. However, their fits are dependent on the shape of the non-thermal proton distribution. As a result we instead use the δ-functional approximation to obtain the injection function of electrons:

$$Q_{e\pm}(E_e) = c\frac{n_p}{K_e}\sigma_{pp}(E_p)N_p(E_p), \tag{B5}$$

where $E_e = K_e E_{kin}$ and K_e is the fraction of the proton energy that the electron has. For electron production via charged pions, $K_e = K_\pi/4$, where $K_\pi = 0.17$ is the fraction of the proton kinetic energy that the
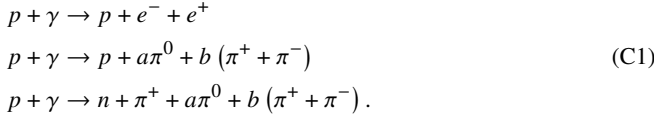
leading pion has. n_p is the number density of thermal protons, and N_p is the distribution function of the non-thermal protons (units of protons $cm^{-3} erg^{-1}$).

The inelastic proton-proton cross section $\sigma_{pp}(E_p)$ can be accurately approximated as (Kelner et al. 2006)

$$\sigma_{pp}(E_p) = \left(34.3 + 1.88\,L + 0.25\,L^2\right)\left[1 - \left(\frac{E_{th}}{E_p}\right)^4\right]^2 \text{ mb.} \quad \text{(B6)}$$

APPENDIX C: CREATION OF SECONDARY PARTICLES AND γ-RAYS VIA PROTON-PHOTON INTERACTIONS

Proton-photon inelastic collisions create pions and electron-positron pairs through the following reactions:

$$\begin{aligned}
p + \gamma &\rightarrow p + e^- + e^+ \\
p + \gamma &\rightarrow p + a\pi^0 + b\left(\pi^+ + \pi^-\right) \quad \text{(C1)} \\
p + \gamma &\rightarrow n + \pi^+ + a\pi^0 + b\left(\pi^+ + \pi^-\right).
\end{aligned}$$

The integer coefficients a and b are, as before, the pion multiplicities. In the rest frame of the proton, the photon threshold energy for the creation of a pair is $\epsilon_{thr}^{\prime(e)} = 2m_e c^2 \approx 1$ MeV. Photomeson production becomes possible when the energy of the photon in the rest frame of the proton is larger than

$$\epsilon_{thr}^{\prime(\pi)} = m_{\pi^0} c^2 \left(1 + \frac{m_{\pi^0}}{2m_p}\right) \approx 145 \text{ MeV}, \quad \text{(C2)}$$

The cross section for pair production is about two orders of magnitude larger than that for pion production. The inelasticity $K_{p\gamma}^{(e)}$, however, is very low, so the proton only loses a small fraction of its energy per collision. As a result, the cooling is completely dominated by pion production if the energy of the photons exceeds $\epsilon_{thr}^{\prime(\pi)}$.

If the cooling of pions and muons before decay is neglected, the injection function of electron-positron pairs can be easily estimated in the δ-functional approximation as in Atoyan & Dermer (2003). Assuming that each charged pion takes an energy $E_\pi \approx 0.2E_p$, and that this energy is equally distributed among the decay products, the energy of each electron/positron is $E_e \approx 0.05\,E_p$. The injection function of pairs is then

$$Q_{e^\pm}(E_{e^\pm}) = 20N_p(20E_e)\,\omega_{p\gamma}^{(\pi)}(20E_e)\,n_{\pi^\pm}(20E_e), \quad \text{(C3)}$$

where $n_{\pi^\pm}$ is the mean number of charged pions created per proton-photon collision and $\omega_{p\gamma}^{(\pi)}$ is the collision rate. Thus the secondary electrons have the same spectral shape as the non-thermal protons and extend up to a maximum energy of $0.05\,E_{p,max}$ where $E_{p,max}$ is the maximum proton energy.

Kelner & Aharonian (2008) provide simple analytical expressions for the spectrum of gamma rays due to decay of neutral pions created in proton-photon collisions. In terms of the distributions of relativistic protons and target photons, the gamma-ray emissivity can be written as

$$q_\gamma^{(p\gamma)}(E_\gamma) = \int_{E_p^{min}}^{E_p^{max}} dE_p \int_{\epsilon_{thr}^{\prime(\pi)}/2\gamma_p}^{\infty} d\epsilon\, \frac{N_p(E_p)}{E_p}\,n_{ph}(\epsilon)\,\Phi(\eta, x). \quad \text{(C4)}$$

Here $\eta = 4\epsilon E_p/m_p^2 c^4$ and $x = E_\gamma/E_p$. The function $\Phi(\eta, x)$ was obtained fitting the numerical results of SOPHIA, a Monte Carlo code for the simulation of photohadronic interactions (Mücke et al.

2000). The function $\Phi(\eta, x)$ can be approximated with an accuracy better than 10% by a simple analytical formula. If we define $x_\pm$ as

$$x_\pm = \frac{1}{2(1+\eta)}\left[\eta + r^2 \pm \sqrt{(\eta - r^2 - 2r)(\eta - r^2 + 2r)}\right], \quad \text{(C5)}$$

then, in the range $x_- < x < x_+$,

$$\Phi_\gamma(\eta, x) = B_\gamma \exp\left\{-s_\gamma\left[\ln\left(\frac{x}{x_-}\right)\right]^{\delta_\gamma}\right\}$$
$$\times \left[\ln\left(\frac{2}{1+y^2}\right)\right]^{2.5+0.4\ln(\eta/\eta_0)}, \quad \text{(C6)}$$

where

$$y = \frac{x - x_-}{x_+ - x_-}, \quad \text{(C7)}$$

and

$$\eta_0 = 2\frac{m_\pi}{m_p} + \frac{m_\pi^2}{m_p^2} \approx 0.313. \quad \text{(C8)}$$

For $x < x_-$, the spectrum is independent of x,

$$\Phi_\gamma(\eta, x) = B_\gamma\,[\ln 2]^{2.5+0.4\ln(\eta/\eta_0)}, \quad \text{(C9)}$$

and $\Phi_\gamma(\eta, x) = 0$ for $x > x_+$. The parameters B_γ, s_γ and δ_γ are functions of η. For values of $1.1\,\eta_0 < \eta < 100\,\eta_0$, these functions are tabulated in Kelner & Aharonian (2008).

For power-law distributions of protons, Kelner & Aharonian (2008) claim that it is more convenient to integrate over $d\eta$. i.e.

$$\frac{dN}{dE} = \int_{\eta_0}^{\infty} H(\eta, E)\,d\eta, \quad \text{(C10)}$$

where

$$H(\eta, E) = \frac{m_p^2 c^4}{4}\int_E^{\infty} \frac{N_p(E_p)}{E_p^2}\,n_{ph}\left(\frac{\eta m_p^2 c^4}{4E_p}\right)\Psi\left(\eta, \frac{E}{E_p}\right)dE_p. \quad \text{(C11)}$$

In practice, we change the integration variable from x to $u = \log_{10}x$.

APPENDIX D: COMPARISON OF ELECTRON AND γ-RAY EMISSION BY PROTON-PROTON AND PROTON-PHOTON INTERACTIONS

Fig. D1 shows the electron and γ-ray spectra produced via proton-proton (pp) and proton-photon (pγ) interactions. In each case the non-thermal protons have a distribution specified by

$$J_p(E_p) = AE_p^{-2}\exp\left(-\frac{E_p}{E_0}\right), \quad \text{(D1)}$$

with $E_0 = 1000$ TeV and A set so that

$$\int_{1\,\text{TeV}}^{\infty} E_p J_p\,dE_p = 1\text{ erg cm}^{-3}. \quad \text{(D2)}$$

The thermal proton density is assumed to be 4×10^5 cm^{-3} (as appropriate for the post-O-shock gas at the stagnation point in the WCR). At this location the secondary star (which dominates the photon flux) occupies a solid angle of $\approx 10^{-6}$ steradian (the stellar radius of the O-star, $R_{*O} = 14.72$ R$_\odot$). It is clear that the proton-proton emissivity is much stronger than the proton-photon emissivity, and that proton-photon emission can be safely ignored in this work.
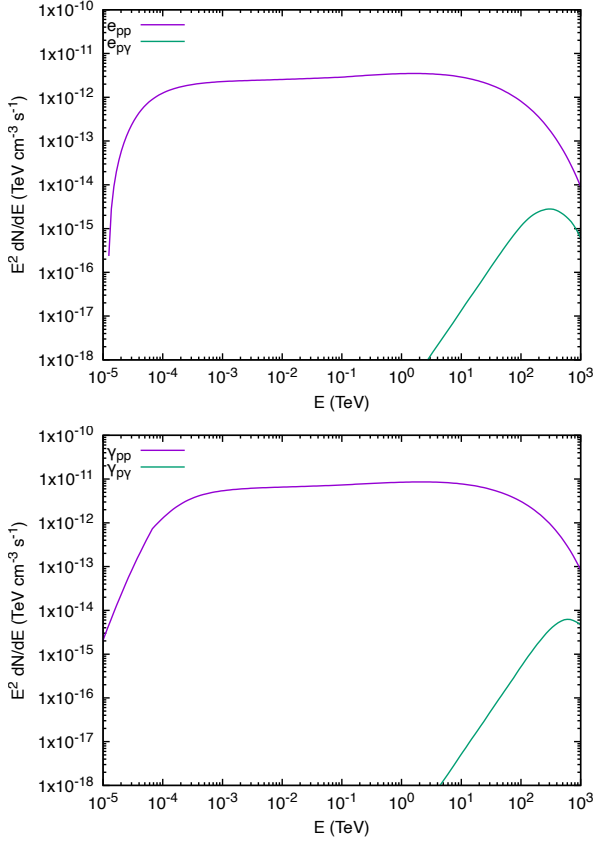
Figure D1. Comparison of the electron (top) and photon (bottom) emissivities for proton-proton and proton-photon interactions. Conditions appropriate for the stagnation point of the WCR are assumed, including a thermal proton number density of $3.9 \times 10^5 \ \mathrm{cm}^{-3}$ and a solid angle of 10^{-6} steradian for the disk of the O-star.

APPENDIX E: SYNCHROTRON EMISSION

The synchrotron power per unit energy radiated by a single electron of energy E_e in a vacuum is given by (e.g. Ginzburg & Syrovatskii 1965; Vila 2012)

$$P_{\rm sync}(E_\gamma, E_e, \alpha) = \frac{\sqrt{3}e^3 B}{m_e c^2 h} \frac{E_\gamma}{E_c} \int_{E_\gamma/E_c}^{\infty} K_{5/3}(\zeta) d\zeta, \qquad (E1)$$

where E_γ is the energy of the emitted photon and $K_{5/3}(\zeta)$ is a modified Bessel function of the second kind. $P_{\rm sync}$ peaks sharply near the characteristic energy

$$E_c = \frac{3heB \sin \alpha}{4\pi m_e c} \gamma_e^2, \qquad (E2)$$

where γ_e is the electron Lorentz factor, and the pitch angle α is the angle between the magnetic field (with flux density B) and the particle's momentum. For a turbulent/isotropic magnetic field, $\sin \alpha = \sqrt{2/3}$. The integral in Eq. E1 can be approximated as (Melrose 1980)

$$x \int_x^\infty K_{5/3}(\zeta) d\zeta \approx 1.85 x^{1/3} e^{-x}, \qquad (E3)$$

where $x = E_\gamma/E_c$ is the dimensionless energy.

The situation changes somewhat if instead the electron is in the presence of a cold background plasma. In such a case the refractive index of the medium, which is smaller than unity, reduces the beaming effect, and can greatly reduce the synchrotron emission. This effect is know as the Tsytovitch-Razin effect (or, more generally, as

the Razin effect; Tsytovitch 1951; Razin 1960). Eq. E1 now becomes (Ginzburg & Syrovatskii 1965; Van Loo, Runacres & Blomme 2004)

$$P_{\rm sync}(E_\gamma, E_e, \alpha) = \frac{\sqrt{3}e^3 B}{m_e c^2 h} f \frac{E_\gamma}{E_c^1} \int_{E_\gamma/E_c^1}^{\infty} K_{5/3}(\zeta) d\zeta, \qquad (E4)$$

where

$$f = \left(1 + \frac{\nu_0^2}{\nu^2} \gamma_e^2\right)^{-1/2}, \qquad (E5)$$

$\nu_0 = \sqrt{n_e e^2/\pi m_e}$ is the plasma frequency, and n_e is the number density of thermal electrons. $E_c^1 = f^3 E_c$.

Eq. E4 may be used for even mildly relativistic electrons, provided that $\chi = \nu/\nu_b \gtrsim 100$, where $\nu_b = \omega_b/2\pi$ and $\omega_b = eB/m_e c$ is the cyclotron frequency of the electron. To capture the transition from cyclotron to synchrotron emission, a data table of emissivity values for $1 < \gamma < 5$ and $10^{-2} < \chi < 2 \times 10^3$ is created using the approach given in Mahadevan et al. (1996).

The photon emission (photon $\mathrm{s}^{-1} \ \mathrm{erg}^{-1}$) is then obtained from integrating over the volume and the distribution of non-thermal electrons:

$$q_{\rm sync}(E_\gamma) = \frac{1}{E_\gamma} \int_V dV \sin \alpha \int_{E_e^{\rm min}}^{E_e^{\rm max}} N_e(E_e) P_{\rm sync}(E_\gamma, E_e, \alpha) dE_e, \qquad (E6)$$

where N_e is the distribution function of the non-thermal electrons (units of electrons $\mathrm{cm}^{-3} \ \mathrm{erg}^{-1}$).

APPENDIX F: PHOTON-PHOTON ABSORPTION BY PAIR CREATION

In CWB systems the stars provide large numbers of target photons for electron-positron pair production with high-energy ($\sim$ TeV) γ-rays. The probability of absorption depends on the cosine of the angle between the directions of the two photons, μ. For a γ-ray of energy E interacting with a stellar photon of energy ϵ, the optical depth is given by

$$\frac{d\tau}{d\epsilon d\Omega dl} = (1 - \mu) n_{\rm ph} \sigma_{\gamma\gamma}, \qquad (F1)$$

where dl is the distance along the path of the γ-ray, $d\Omega$ is the solid angle of the stellar surface, and $n_{\rm ph}$ is the radiation density which is assumed to be that of a blackbody of temperature T_*:

$$n_{\rm ph} = \frac{2\epsilon^2}{h^3 c^3} \frac{1}{\exp(\epsilon/(kT_*)) - 1} \qquad (\mathrm{ph \ cm}^{-3} \ \mathrm{erg}^{-1} \ \mathrm{sr}^{-1}). \qquad (F2)$$

The cross-section depends only on $\beta = (1 - 1/s)^{1/2}$, where $s = \epsilon/\epsilon_{\rm min}$ and the threshold energy

$$\epsilon_{\rm min} = \frac{2m_e^2 c^4}{E(1 - \mu)}. \qquad (F3)$$

The cross-section is (Gould & Schréder 1967)

$$\sigma_{\gamma\gamma}(\beta) = \frac{3}{16} \sigma_{\rm T}(1 - \beta^2) \left[(3 - \beta^4)\ln\left(\frac{1 + \beta}{1 - \beta}\right) - 2\beta(2 - \beta^2)\right]. \qquad (F4)$$

We follow the prescription given in Dubus (2006) to calculate the opacity (see also Romero, del Valle & Orellana 2010). The integral over solid angle can be split into one over μ and ϕ. As noted by Dubus (2006), the energy integral can be replaced with a definite integral over β between the limits [0,1] while the integral along l

can be replaced with a definite integral over the angle ψ between the limits $[\psi_0, \pi]$. The final equation for calculating the optical depth then becomes

$$\tau = \int_{\psi_0}^{\pi} \frac{d_0 \sin \psi_0}{\sin^2 \psi} d\psi \int_{\mu_{\min}}^{1} d\mu \int_0^{2\pi} d\phi$$

$$\times \int_0^1 \frac{2\epsilon^2 \sqrt{1-\beta}}{\epsilon_{\min}} (1-\mu) n_{\rm ph} \sigma_{\gamma\gamma} d\beta, \quad \text{(F5)}$$

where $\mu_{\min} = (1 - R_*^2/d^2)^{1/2}$ and d is the distance of the γ-ray to the star.

APPENDIX G: FREE-FREE ABSORPTION

The emission from the WCR can also be absorbed by the stellar winds. In our axisymmetric model, the line of sight to the observer from a given patch on the WCR may pass solely through the primary or secondary wind, or it may pass first through the secondary wind and then move into the primary wind[10].

The dot product of the line of sight vector with the normal to the shock determines if the line of sight moves into the primary wind or into the secondary wind. If the latter occurs the line of sight may remain in the secondary wind, or it may intersect another part of the WCR and then move into the primary wind. To determine if this latter case occurs, a triangle or quadrangle facet is constructed from each patch on the WCR. Triangular facets are constructed only for those patches that touch the apex of the WCR, while quadrangles are constructed for all other patches. The list of triangle and quadrangle facets is then run through to find intersections with the line of sight, using standard techniques (Schlick & Subrenat 1993; Möller & Trumbore 1997).

For an ionized stellar wind consisting solely of protons and electrons the optical depth due to free-free absorption along a line of sight, s, is given by (see Wright & Barlow 1975; Panagia & Felli 1975)[11]

$$d\tau = \int_{s_0}^{s_1} n^2 K ds = n_0^2 K \int_{s_0}^{s_1} \frac{ds}{s^2 + q^2} = \frac{n_0^2 K}{2q^3} \left[\frac{qs}{d^2} + \tan^{-1}\left(\frac{s}{q}\right) \right]_{s_0}^{s_1}.$$

$$\text{(G1)}$$

Here the proton (and electron) number density is

$$n = \frac{n_0}{s^2 + q^2}, \quad \text{(G2)}$$

with

$$n_0 = \frac{\dot{M}}{4\pi v_\infty m_{\rm H}}. \quad \text{(G3)}$$

The line of sight ray has an impact parameter q with the star, $s = 0$ at the point of closest approach to the star, and the observer is at $s = +\infty$. In Eq. G1, s_0 is the starting point of the ray and s_1 is either equal to $+\infty$ or the value obtained at the intersection point of the WCR. In the latter case the total opacity is obtained from $\tau = d\tau_1 + d\tau_2$, where $d\tau_1$ and $d\tau_2$ are the optical depths through each wind along the line of sight.

In cgs units, K is given by (Wright & Barlow 1975)

$$K = 3.7 \times 10^8 [1 - \exp(-h\nu/kT)] g(\nu, T) T^{-1/2} \nu^{-3} \quad \text{cm}^5, \quad \text{(G4)}$$

where g is the Gaunt factor. K is appropriately scaled for a wind with other atomic species. In evaluating K we assume that the wind temperature is maintained at 10^4 K. Hydrogen and helium are assumed to be singly ionized while C, N and O are assumed to be doubly ionized. The relative number densities of H, He and CNO are assumed to be given by X, $Y/4$ and $Z/14.24$. Finally, if the wind is clumpy, Eq. G1 is scaled by $1.0/f$, where f is the volume filling factor of the clumps ($f < 1.0$).

Additional absorption due to the material in the WCR can also be included, if desired (see, e.g., Parkin & Pittard 2008). However, this addition is only likely to be significant if the WCR strongly cools, and so is not included in the present work.

This paper has been typeset from a TeX/LaTeX file prepared by the author.

---

[10] If orbital motion is included, the WCR obtains a spiral shape, and multiple transitions between primary and secondary wind material may occur along each line of sight - see Parkin & Pittard (2008).

[11] There is an equivalence between the geometry used by Wright & Barlow (1975) and Panagia & Felli (1975) for the free-free absorption, and Dubus (2006) for the photon-photon absorption.